Atmospheric Research 277 (2022) 106290

Contents lists available at ScienceDirect

Atmospheric Research

journal homepage: www.elsevier.com/locate/atmosres

Performance assessment of aerosol-lidar remote sensing skills to retrieve the time evolution of the urban boundary layer height in the Metropolitan Region of São Paulo City, Brazil

Gregori de Arruda Moreira [a,b,c,*], Amauri Pereira de Oliveira [b], Maciel Piñero Sánchez [b], Georgia Codato [b], Fábio Juliano da Silva Lopes [c], Eduardo Landulfo [c], Edson Pereira Marques Filho [d]

[a] *Instituto Federal de São Paulo (IFSP), Registro, São Paulo, Brazil*
[b] *Department of Atmospheric Sciences, University of São Paulo, São Paulo, São Paulo, Brazil*
[c] *Institute of Nuclear Energy Research, São Paulo, São Paulo, Brazil*
[d] *Interdisciplinary Center for Energy and Environment, Federal University of Bahia, Salvador, Bahia, Brazil*

ARTICLE INFO

Keywords:
Elastic lidar
Remote sensing systems
Urban boundary-layer

ABSTRACT

This paper investigates the performance of seven methods of retrieving the planetary boundary layer height (*PBLH*) from lidar measurements carried out in the Metropolitan Region of São Paulo (*MRSP*) during two *MCITY-BRAZIL* field campaigns of 2013. The performance is objectively assessed considering as reference the *PBLH* retrieved from rawinsonde carried out every 3 h during these campaigns. The role of clouds and aerosol load in the performance of the seven methods is analysed considering three case study scenarios representative of typical atmospheric conditions in the *MRSP*: (a) winter clean atmosphere, (b) summer low clouds and aerosol multi-layers, (c) summer sea-breeze intrusion. Corroborating the case study results, the objective analysis indicated that most of the lidar methods retrieved *PBLH* closer to the top of the entrainment zone than the mixed layer, contradicting their definition. During daytime, the Wavelet Covariance Transform Method performs better than all the other six methods. The Inflexion Point Method performed better to estimate the Residual Layer height during night-time. In average, the diurnal evolution of the *PBLH* and its local rate of change based on lidar and rawinsonde measurements are in agreement.

1. Introduction

Basic properties of the Urban Boundary Layer (*UBL*) over tropical cities are not very well documented (Sánchez et al., 2020). In tropical regions, most of the local networks of upper-air monitoring stations are sparse, rawinsonde data have low vertical (~300 *m*) and temporal (~12 h) resolutions. In general, sounding releases twice-a-day at fixed universal times, yielding a fragmented description of the *UBL* properties. This is particularly problematic in places like Brazil where soundings are performed at 0900 and 2100 Local Time (*LT*), when the convective and stable turbulent regime are still incipient (Sánchez et al., 2020).

In the last two decades remote sensing systems have been widely applied in Planetary Boundary Layer (*PBL*) studies. Although the combination of equipment and algorithms have been applied in this kind of study (Bianco and Wilczak, 2002; Tucker et al., 2009; Bonin et al., 2018), there are still uncertainties associated with equipment (e.g., signal-to-noise ratio (Kotthaus et al., 2016; Kotthaus et al., 2020)) and retrieving techniques limitations (e.g., rainy, cloudy, or Sahara dust outbreak situations (Bravo-Aranda et al., 2017; Cazorla et al., 2017; Kotthaus et al., 2020)) that need to be identified facing the great diversity of atmospheric conditions resulting from its popularization (Bonin et al., 2018). Considering the remote sensing instruments, the elastic lidar is one of the most used to retrieve properties of the *PBL*, due to reliability and a wide range of approaches to its results (Davis et al., 2000; Brooks, 2003; Morille et al., 2007; Baars et al., 2008; Pal et al., 2010; De Tomasi et al., 2011; Granados-Muñoz et al., 2012; Wang et al., 2012; Lange et al., 2014; Banks et al., 2016; Bravo-Aranda et al., 2017; Lopes et al., 2014; Moreira et al., 2018; Liu et al., 2019; Cimini et al., 2020; Moreira et al., 2019; Vishnu et al., 2021; Moreira et al., 2022). They use aerosols as tracers to estimate the *PBL* Height (*PBLH*) as the

---

* Corresponding author at: Instituto Federal de São Paulo (IFSP), Registro, São Paulo, Brazil.
E-mail address: gregori.moreira@ifsp.edu.br (G.A. Moreira).

https://doi.org/10.1016/j.atmosres.2022.106290
Received 10 November 2021; Received in revised form 24 May 2022; Accepted 6 June 2022

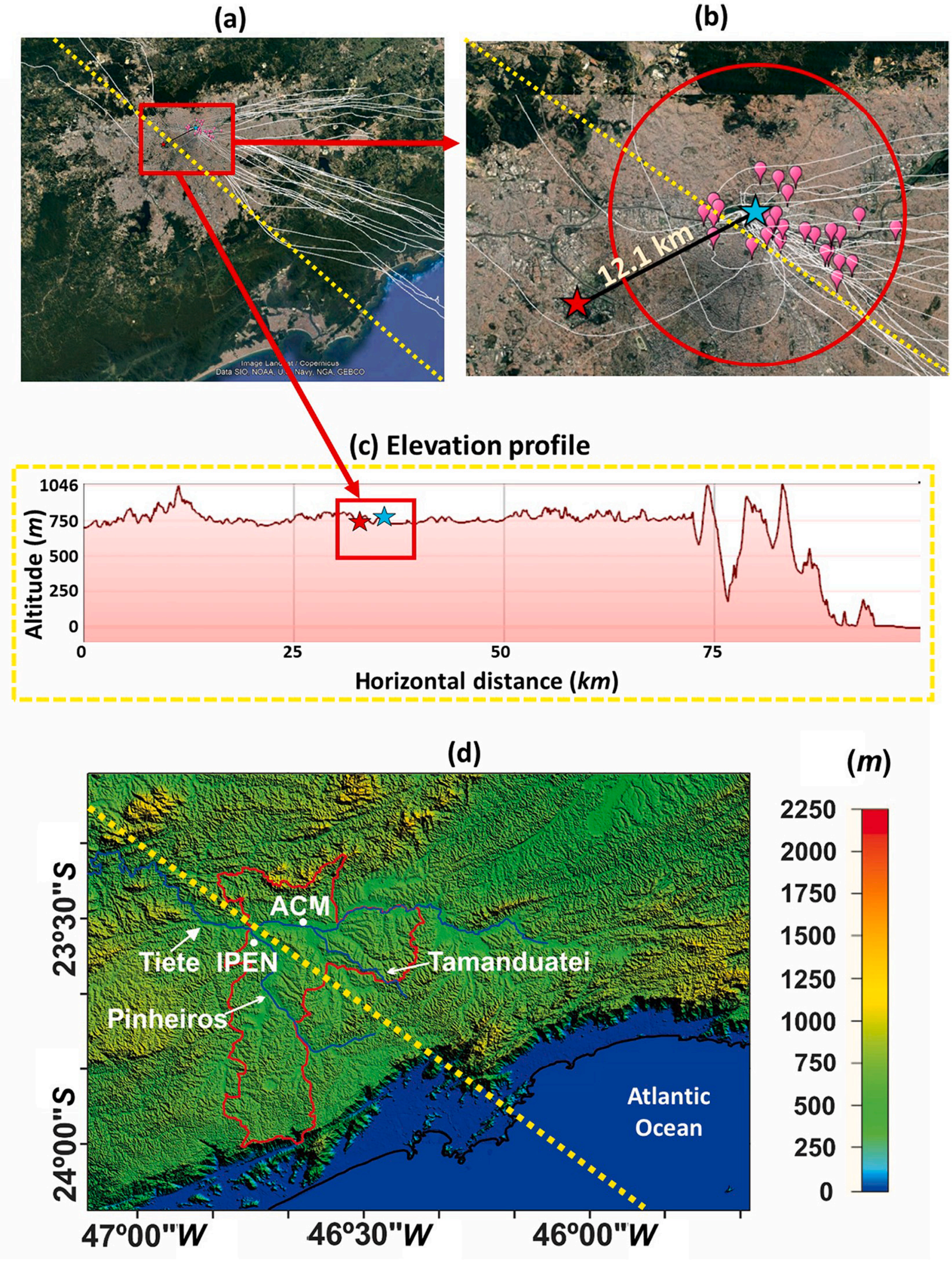

Fig. 1. (a) *MRSP* Map. (b) Geographic position of lidar (*IPEN*, red star) and rawinsonde (Campo de Marte Airport, cyan star) sites with respect to land. (c) Elevation profile (yellow dotted lines in (a), (b) and (d). (d) *RMSP* topography. The white lines in (a) and (b) indicate the trajectory of each rawinsonde. The pink balloons in (b) represent the horizontal position where rawinsondes reached the height of 4000 *m*. The yellow dotted (radius = 7 *km*) circle in (b) indicates the area covered by rawinsondes until they reach 4000 *m*. Topography in (d) is based on the highest-resolution topographic data (3-arc-second Resolution - 90 m) generated from *NASA*'s Shuttle Radar Topography Mission (*SRTM*), available at https://www2.jpl.nasa.gov/srtm/. The geographic limits of São Paulo City are indicated by red in (d). (For interpretation of the references to colour in this figure legend, the reader is referred to the web version of this article.)

midpoint between transition layers of high and low backscattering intensity. Under ideal conditions (undisturbed synoptic conditions, clear skies, flat topography and homogeneous land use) and during daytime this transition is within the Entrainment Zone (*EZ*) (a stable layer at the top of Mixed Layer (*ML*) and below Free Atmosphere (*FA*) (Stull, 1988; Wyngaard, 2010)). During night-time the transition is within the former Capping Inversion, which is situated above the Residual Layer (*RL*) (Stull, 1988; Wyngaard, 2010). Under more realistic conditions, finding this midpoint in a lidar signal is not an easy task because the vertical distribution of aerosol in the lower atmosphere is strongly dependent of local meteorological conditions and may display a complex behaviour (Kovalev and Eichinger, 2004). Consequently, several methods have been developed to estimate the *PBLH* based on different strategies to reduce ambiguities of complex situations such as aerosol multilayers, clouds, etc. (Kovalev and Eichinger, 2004).

In this work, seven *PBLH* detection methods are applied to estimate daytime evolution of *UBL*, for the first time, in the Metropolitan Region of São Paulo (*MRSP*) using a mobile Raman lidar measurements carried out during two field campaigns of the *MCITY* (MegaCITY) *BRAZIL* Project in 2013 (Oliveira et al., 2020). These methods are: (1) Variance (Emeis, 2011), (2) Gradient (Flamant et al., 1997), (3) Logarithmic Gradient (Senff et al., 1996), (4) Inflexion Point (Menut et al., 1999), (5) Threshold (Melfi et al., 1985), (6) Ideal Curve-Fitting (Steyn et al., 1999), and (7) Wavelet Covariance Transform (Baars et al., 2008). The performance of these methods is assessed objectively using as reference the height of the *ML* (*MLH*), *EZ* (*EZH*), and *RL* (*RLH*), estimated previously from fine resolution rawinsonde by Sánchez et al. (2020). Experimental site and measurements are described in Section 2, the methodology in Section 3, results are discussed in Section 4 and conclusions are given in Section 5.

2. Experimental site and measurements

Observations used in this work are based on lidar and rawinsonde measurements carried out in the *MRSP* during two field campaigns of the *MCITY-BRAZIL* project in 2013. This project started in 2013 with the implementation of a network of three micrometeorological towers in sites representative of urban, suburban, and rural land use of the *MRSP*, where surface energy and radiation budget components are measured since 2013 (Oliveira et al., 2020).

The *MRSP* consists of an urban area of 7947 km^2 (Fig. 1a), occupied by approximately 21.3 million inhabitants. It is composed of thirty-nine cities, most of them located in the Paulista Plateau at 700 *m* above sea level (*asl*) and about 60 *km* from the Atlantic Ocean. The entire urban portion of the *MRSP* is in the Paulista Plateau, limited at the north and northwest by a chain of ridges of up to 700 m. The *MRSP* is characterized by three major valleys: the Tiete River, oriented in the east-west direction; Tamanduatei River, oriented in the northwest-southeast direction, and Pinheiros River, oriented in the northeast-southwest direction (Fig. 1d). The São Paulo City is the core city of the *MRSP* (Fig. 1d), it comprises 1507 km^2 of land with approximately 11.9 million inhabitants and population density of 7900 people per square kilometres (Oliveira et al., 2020). The climate of São Paulo is classified as high elevation subtropical humid (*Cwb*), with dry and mildly cold winters (June–August), and wet and warm summers (December–February).

Each field campaign lasted 10 days and consisted of launching rawinsonde every 3 h, from the *"Campo de Marte"* Airport (23°30′32" *S*, 46°38'04" *W*, 722 *m asl*) at northern São Paulo City. Two sets of 80 soundings each were performed during summer (February 19 to 28, 2013) and during winter (August 6 to 15, 2013), respectively. In Section 3 is presented an analysis about the *ML* and *EZ* behaviour considering all 139 valid rawinsondes. On the other hand, in Section 4 is presented a comparison between lidar data and 29 rawinsondes, corresponding to a total of 11 days (8 in winter [August 8 to 15] and 3 in summer [February 20 to 22] field campaigns) when the Metropolitan São Paulo (*MSP*) Lidar 2 was in operation.

2.1. Lidar

The *MSP* Lidar 2, is a mobile biaxial ground-based multiwavelength Raman lidar system. It operates with a pulsed *Nd:YAG* laser in one elastic channel (532 *nm*) and one Raman-shifted channel (607 *nm* – from Nitrogen), that reaches full overlap around 180 *m* above ground level. In both field campaigns, *MSP* Lidar 2 system operated, from 1000 *LT* to 2100 *LT*, retrieving vertical profiles of the backscatter raw signal (*P*) every 50 s with a spatial resolution of 7.5 *m* from the level of 180 *m* (full overlap) and composed by 1000 laser shots sampled at a rate of 20 *Hz*. This system belongs to Laser Environmental Applications Laboratory which is part of Latin America Lidar Network – *LALINET* (Guerrero-Rascado et al., 2016; Antuña-Marrero et al., 2017). This Lidar was in operation in the Institute of Research and Nuclear Energy (*IPEN*) located in the University of São Paulo campus, west São Paulo City (23°33′38" *S*, 46°44′21" *W*, 757 *m asl*), approximately 12.1 *km* far from the "*Campo de Marte*" Airport where the rawinsondes were released (Fig. 1).

2.2. Rawinsonde

Rawinsonde performed at the "*Campo de Marte*" Airport uses an upper air rawinsonde system manufactured by Vaisala Inc. It is composed by a *DIGICORA III* data acquisition system set up with a sampling frequency of 0.1 *Hz* and the rawinsonde model *RS92-GSP*. Ground-checking procedure was carried out using a surface meteorological station from the "*Campo de Marte"* Airport as the ground reference. The initial ascend velocity of rawinsonde was about 5.5 $m\,s^{-1}$ and the vertical resolution prevailed between 60 and 70 *m* (Sánchez et al., 2020).

A trajectory analyses of all rawinsonde released during both field campaigns indicate that up to 4000 *m* they were within the urban limits of *MRSP*, sampling thermodynamic and dynamic properties of the atmosphere in a 4000 *m* column with circular area of radius varying from 7 to 14 *km* (Sánchez et al., 2020). This indicates that the properties described by these rawinsondes can be assumed as representative of the *UBL* in *MRSP*. Even though Lidar measurements are performed at 12.1 *km* far from the rawinsonde launching site (Fig. 1b), both experimental sites are inside the urban region of the *MRSP* with similar land use, far from urban borders and chain of ridges at north (Fig. 1a) and separated by small hills and valleys (∼ 100 *m*) (Fig. 1c). Besides, Lidar measurements was located either very close or inside the circular area (radius = 7 *km*) sampled by the rawinsondes. Therefore, it is plausible to assume that any difference between the *UBL* (and *RL)* height retrieved from lidar and rawinsonde measurements are not due to land use and topographic effects, nor to the lack of spatial representativeness of rawinsonde measurements. As consequence, any significant difference between the *UBL* and *RL* heights estimated from lidar and rawinsonde will be associated exclusively to limitations of the lidar methods in to cope with local atmospheric effects on the *PBL* structure induced by the presence of low clouds, aerosol multilayers and sea-breeze intrusion in the *MRSP*.

3. Methodology

3.1. Lidar methods

The raw lidar signal *P(z)* is given by the following equation:

$$P(z) = P_0\frac{ct_d}{2}AO(z)\frac{\beta(z)}{z^2}exp\left[-2\int_0^z \alpha(z')dz'\right] \tag{1}$$

where P_0 is the power of emitted laser pulse, *c* is the light speed ($m\,s^{-1}$), t_d is the duration of laser pulse (*ns*), *A* is the area (m^2) of telescope cross section, $O(z)$ is the overlap function, $\beta(z)$ is the total backscatter coefficient [$(km\ sr)^{-1}$] at distance z and $\alpha(z)$ the total extinction coefficient (km^{-1}) at distance z.

Lidar methods of retrieving *PBLH* are based on the variation of *RCS* (Range Corrected Signal) profiles (Kovalev and Eichinger, 2004), which are obtained from the following equation:

$$RCS(z) = (P(z) - DC(z) - BG)\,z^2 \tag{2}$$

The dark current signal ($DC(z)$) and background radiation signal (BG) are subtracted of ($P(z)$) to reduce the influence of electrical noise and to attenuate the influence of external sources, respectively. Then, due to attenuation of the lidar signal with the height, the result of subtractions is multiplied by the square of the corresponding height (z) (D'Amico et al., 2016). The *RCS* is represented by Arbitrary Units (*au*).

In the absence of clouds, Kovalev and Eichinger (2004) combined Eq. (1) and Eq. (2) to demonstrate that a drop in the aerosol concentration (ΔC) along the *EZ* is proportional to a drop in the *RCS* profile (ΔRCS), caused by variation in the total backscatter ($\Delta\beta$) and extinction ($\Delta\alpha$) coefficients as indicated by:

$$\Delta C \sim \Delta RCS \sim f_a[\beta, \alpha] \tag{3}$$

where f_a is an empirical function.

Due to the spatial and temporal variability of the aerosol concentration along the *PBL* to identify the *PBLH* based on *RCS* profile is not an easy task, demanding special mathematical techniques to cope with complex situations.

In this section, seven methods of estimating *PBLH* from *RCS* profiles are summarized. These methods are applied to vertical profiles of mean ($\overline{RCS}$) and variance $\sigma^2_{RCS}(z)$ of *RCS*, both composed of 12 consecutive profiles of *RCS* observed at 10-min intervals. This procedure was defined empirically to mitigate the influence of instrumental noise and provide a more reliable estimate of *PBLH* without losing the high temporal resolution of lidar systems. As it will be discussed in this section, all seven methods present some difficulties to estimate the *PBLH* in situations associated with the presence of clouds, and aerosol multilayers.

3.1.1. *Variance method (VM)*

In this method the $PBLH_{VM}$ is identified as the height of the maximum in the variance profiles of *RCS* observed during 10-min intervals. In this case the variance is given by:

$$\sigma^2_{RCS}(z) = \frac{1}{n}\sum_{i=1}^{n}\left[RCS_i(z) - \overline{RCS}(z)\right]^2 \tag{4}$$

where *n* (=12) is the number of the *RCS* profiles observed during 10-min intervals.

For clear sky and convective conditions, this maximum occurs at *ML* top, due to the entrainment of clean air from *FA*. The presence of cloud-base and aerosol multilayers above (or below) the top of the *ML* generates peaks in the variance profiles, which are not associated with the process mentioned above, causing incorrect estimation of *PBLH* (Emeis, 2011). In these cases, the *PBLH* is unrealistic high (or low), because it estimates the cloud-base or aerosol multilayer-top height.

3.1.2. *Gradient-based methods*

These methods estimate *PBLH* as the height where occurs a significant reduction in the aerosol concentration between *ML* top and *FA*. This reduction is identified using gradient properties of *RCS* profiles. The most applied gradient methods are described hereafter.

3.1.2.1. *Gradient method (GM).*

The $PBLH_{GM}$ corresponds to the height of the first local minimum in the $\overline{RCS}(z)$ profile indicated by:

$$PBLH_{GM} = Min\left[\frac{d\overline{RCS}(z)}{dz}\right] \tag{5}$$

According to Flamant et al. (1997), $PBLH_{GM}$ corresponds to *MLH*.

3.1.2.2. *Logarithmic gradient method (LGM).*

The $PBLH_{LGM}$ corresponds to the height of the first local minimum in the natural logarithm of $\overline{RCS}(z)$ profile given by:

$$PBLH_{LGM} = Min\left[\frac{d\ln\left(\overline{RCS}(z)\right)}{dz}\right] \tag{6}$$

This method causes a linearization in the extinction coefficient (α) in the Eq. (2), increasing the difference between maximum and minimum values in the gradient the $\overline{RCS}(z)$ profile (Martucci et al., 2007). According to Senff et al. (1996), the local minimum in the natural logarithm of $\overline{RCS}(z)$ profile corresponds to the height of the *ML* top. Therefore, $PBLH_{LGM}$ is a considered a good estimator for *MLH*.

3.1.2.3. *Inflexion point method (IPM).*

The $PBLH_{IPM}$ is the height of the inflexion point of $\overline{RCS}(z)$ profile. It corresponds to the first minimum of the second derivative of $\overline{RCS}(z)$:

$$PBLH_{IPM} = Min\left[\frac{d^2\overline{RCS}(z)}{dz^2}\right] \tag{7}$$

According to Menut et al. (1999), the first minimum of the second derivative of $\overline{RCS}(z)$ corresponds to the middle of *EZ*. Therefore, it is reasonable to assume that $MLH < PBLH_{IPM} <$ height of the *EZ* top (*EZH*).

3.1.3. *Threshold method (TM)*

This method estimates $PBLH_{TM}$ as the height where $\overline{RCS}(z)$ becomes lower than a predetermined threshold (Melfi et al., 1985). There is not a standard value for this threshold varying in accordance with each region and/or instrument. While Boers et al. (1988) used 25% of the maximum *RCS* value, Frioud et al. (2003) applied $4.10^{-4}\ m^{-1}$. In this work it will be considered a threshold equal to 80% of the maximum of $\overline{RCS}$ profile, estimated by trial-and-error (Moreira et al., 2013), $PBLH_{TM}$ can be expressed as:

$$PBLH_{TM} = z, where\ \overline{RCS}(z) < Max\left(\overline{RCS}\right)*0.8 \tag{8}$$

The reduction in the $\overline{RCS}$ is due to decrease of aerosol concentration in the transition between *ML* and *FA*. Therefore, it is also reasonable to assume that $MLH < PBLH_{TM} < EZH$.

Although easy to apply, the *TM* may retrieve unrealistic $PBLH_{TM}$ values due to the threshold inherent randomness existing in the trial-and-error selection procedure caused, mainly, through natural variability of the atmosphere (Kovalev and Eichinger, 2004).

3.1.4. *Ideal curve-fitting method (ICM)*

In this method the $PBLH_{ICM}$ is estimated as the height of the inflexion point of an ideal $\overline{RCS}$ profile:

$$\overline{RCS}(z) = \frac{RCS_m + RCS_u}{2} - \frac{RCS_m - RCS_u}{2}\ erf\left(\frac{z-h}{\Delta h}\right) \tag{9}$$

fitted through observed $\overline{RCS}$ profile, where RCS_m is the mean value of the $\overline{RCS}$ in the *ML*, RCS_u is the mean $\overline{RCS}$ value in the region above the *ML*, *z* represents heights, *h* is the top of *ML*, and Δh is the thickness of the *EZ* (Steyn et al., 1999).

All these unknow parameters (RCS_m, RCS_u, Δh, *h*) are obtained using an iterative selection procedure based on multidimensional minimization technique proposed by Steyn et al. (1999). In this method $PBLH_{ICM}$ corresponds to the middle of *EZ* ($MLH < PBLH_{ICM} < EZH$).

3.1.5. *Wavelet covariance transform (WCT)*

The $PBLH_{WCT}$ is detected by the maximum in function *W(a,b)*:

$$W(a,b) = \frac{1}{a}\int_{z_i}^{z_f}\overline{RCS}(z)h\left(\frac{z-b}{a}\right)dz \tag{10}$$

where z_i and z_f are the lower and upper limits of the $\overline{RCS}(z)$, $h\left(\frac{z-b}{a}\right)$ - the Haar function - is the mother wavelet, and *a* is the dilation and *b* the transition.

The function *W(a,b)* is the covariance between the normalized $\overline{RCS}$ and the mother wavelet. The *W(a,b)* maximum correspond to the sharpest drop in the $\overline{RCS}$ profile, which represents the top of *ML* (Baars et al., 2008). Therefore, the $PBLH_{WCT}$ correspond to *MLH*. The selection of *a* and *b* represents a significant challenge in the application of the *WCT* method. These parameters are linked to the vertical distribution of *RCS*, that varies with the aerosol load and atmospheric conditions. Based on a previous study of Moreira et al. (2014) the parameters *a* and *b* received the values 200 and 40 *m*, respectively.

3.2. *Rawinsonde method*

In this work, the UBL properties such as *MLH, EZH*, and RLH were estimated previously by Sánchez et al. (2020) applying visual inspection

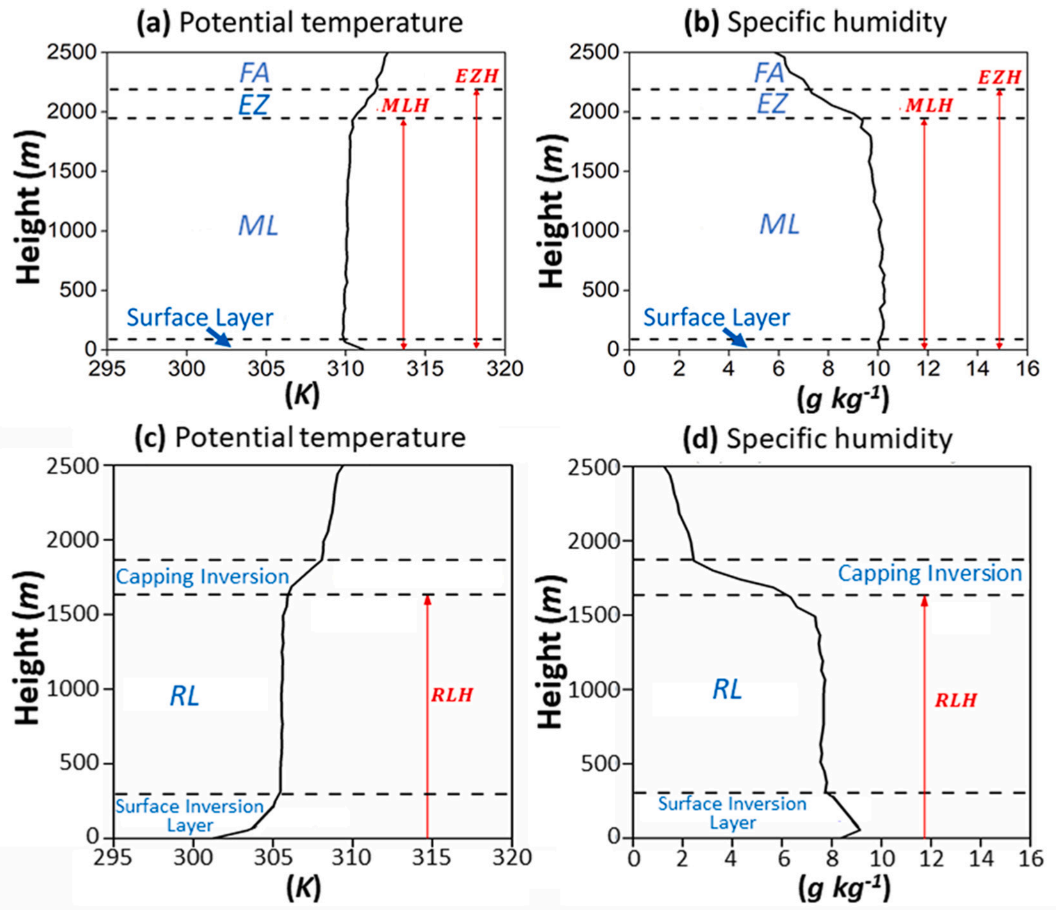

Fig. 2. Vertical profiles of (a)-(c) Potential temperature and (b)-(d) Specific humidity indicating the structures used as reference during day (*EZH*, *MLH*) and night (*RLH*) by Sánchez et al. (2020). They are based on rawinsonde carried out on (a)-(b) February 20, 2013, at 1500 *LT*, (c)-(d) August 9, 2013, at 2100 *LT* in the *MRSP*.

method to rawinsonde carried out during the MCITY-BRAZIL project in February 19–28 (Summer) and August 6–15 (Winter) in the MRSP. This method consists of visually comparing observed and expected structures, using as the reference of expected structure profiles of potential temperature and specific humidity observed under undisturbed conditions (Fig. 2). As indicated in this figure, during daytime the expected structure consists of three adjacent layers: the surface layer (*SL*), a shallow layer adjacent to the surface where the potential temperature and specific humidity decrease with height; the *ML*, where these properties are constant; and the *EZ*, where potential temperature increases, and specific humidity decreases with height at a rate larger than in the *FA* immediately above. During night-time the expected structure consist of two layers: the Surface Inversion (*SI*) layer adjacent to the surface, where the potential temperature increases and specific humidity (excepted by a thin saturated layer beneath) decreases with height; the *RL* immediately above the *SI* layer, remaining of the daytime *ML*. In the case of the RMSP, due to the strong thermal stratification of the *SI* layer, the Stable Boundary Layer height (*SBLH*) was systematically lower than the *SIH* during the field campaigns of 2013 (Section 4.1). The *SBLH* was not indicated in Fig. 2, nor identified by Sánchez et al. (2020), because the effect of turbulence in the vertical distribution of potential temperature and specific humidity could not be clearly identified using rawinsondes with vertical resolution of 62 m. According to the reference structure used by Sánchez et al. (2020), during daytime the top of the *UBL*(*PBLH*) corresponds to *EZH* (Fig. 2).

The performance of the visual method was investigated by Sánchez et al. (2020) using *PBLH* retrieved by three objective methods as reference: Richardson Number (Zhang et al., 2013), Gradient (Moreira et al., 2020) and Air Parcel (Holzworth, 1964). They found a Willmott index of agreement (defined in Section 4) equal to 0.83 for Richardson Number method; 0.85 for Gradient method; and 0.88 for Air Parcel method. These results indicate that there is a good agreement between *PBLH* retrieved visually and by objective methods. Therefore, it seems reasonable to assume that the other *UBL (MLH)* and *RL* (*RLH*) properties obtained by Sánchez et al. (2020), and used here as reference, have an equivalent accuracy.

3.3. Comparison among rawinsonde and lidar methods

In this section the performance of the seven lidar methods are assessed using as reference rawinsonde estimates of *MLH*, *EZH* and *RLH*. This assessment is based on the difference among *PBLHs* and *RLH* retrieved by all seven lidar methods and rawinsonde data as indicated below:

$$\text{Difference} = \Delta_X \begin{cases} PBLH_Y - Z \\ RLH_Y - RLH_{rawinsonde} \end{cases} \tag{11}$$

Where *X* indicates *ML*, *EZ*, or *RL*, *Z* indicates the *MLH* or the *EZH* obtained from rawinsonde, and *Y* indicates the seven lidar methods: *VM* (Variance), *ICM* (Ideal Curve-Fitting), *IPM* (Inflexion Point), *LGM* (Logarithmic Gradient), *GM* (Gradient), *TM* (Threshold), and *WCT* (Wavelet Covariance Transform). This analysis is based on 29 rawinsondes, launched during the 11 days of valid lidar measurements, at three distinct moments representative of different stages in the diurnal evolution of the *UBL* in the *MRSP*: fast-growing at 1200 *LT*, mature at 1500 *LT*, convective-stable transition at 1800 *LT*. The analysis includes rawinsonde released at 2100 *LT* to assess the performance of the lidar methods to retrieved *RLH*. The rawinsondes launched at 0900 *LT* were

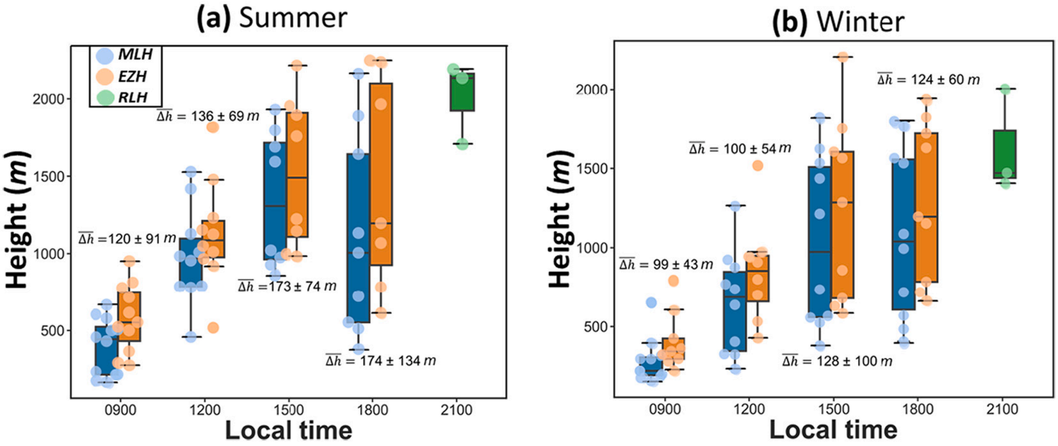

Fig. 3. (a) summer and (b) winter diurnal evolution of the boxplot-statistics of *MLH* (blue), $PBLH_{EZ}$ (orange), *RLH* (green), and mean and standard deviation of the difference $PBLH_{EZ}$ - *MLH*, indicated by $\overline{\Delta h}$. The light blue, orange and green dots represent the values of *MLH*, *EZH*, and *RLH*, respectively. They are based on rawinsonde carried out every three hours during summer and winter field campaigns of the *MCITY*-BRAZIL project in *MRSP*. *(For interpretation of the references to colour in this figure legend, the reader is referred to the web version of this article.)*

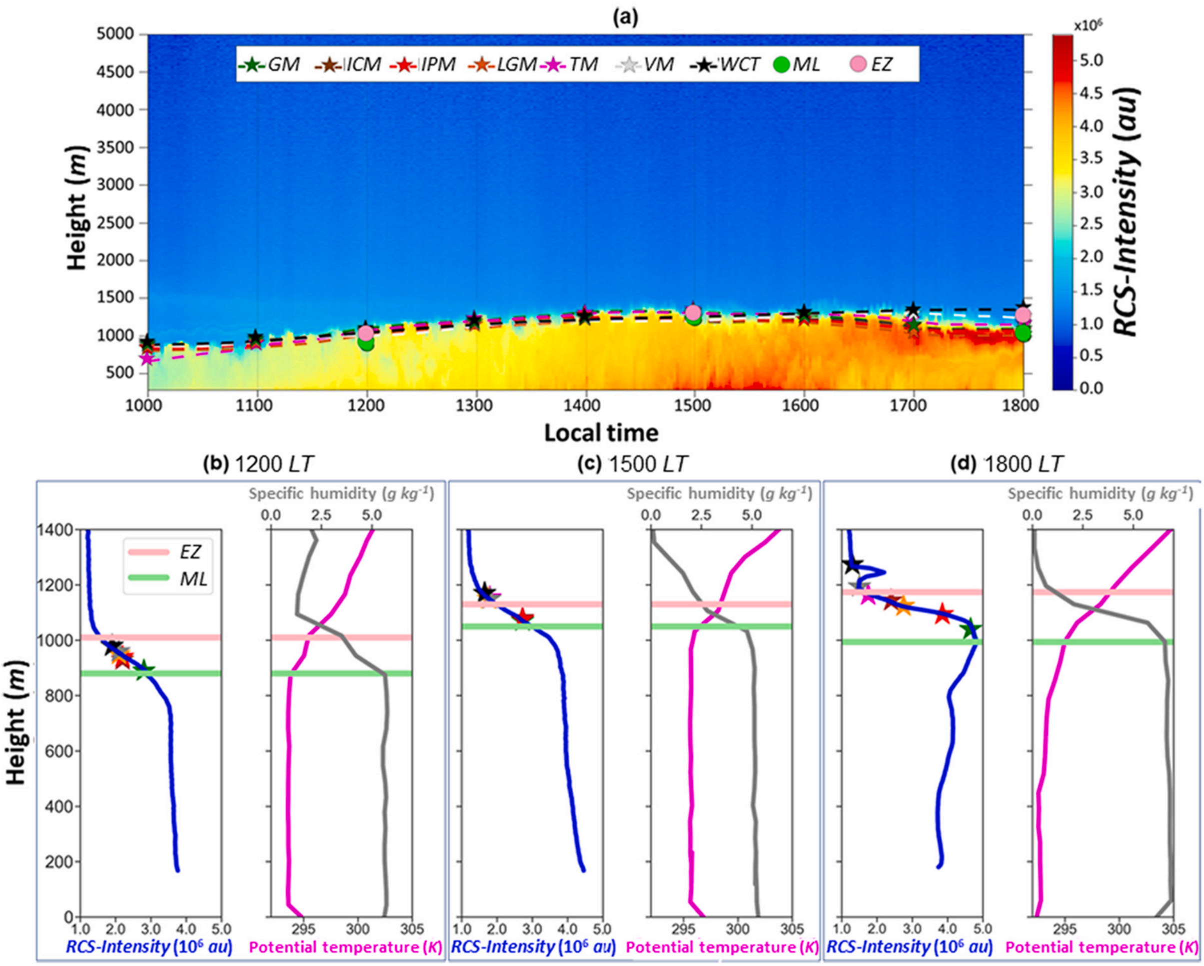

Fig. 4. (a) *RCS-Intensity* contour plot on August 11, 2013 (Case I – Winter clean atmosphere). The solid-star dashed-lines in (a) indicate the *PBLH*s obtained from lidar methods, and solid circles indicate *MLH* (light green, *ML*) and *EZH* (pink, *EZ*) obtained from rawinsonde data. Vertical profiles of *RCS-Intensity* (blue line), potential temperature (magenta line) and specific humidity (grey line) in (b)-(d) correspond, respectively, to measurements at 1200, 1500, and 1800 *LT*. The solid stars in the *RCS-Intensity* profiles indicate the *PBLH*s obtained from lidar methods, and horizontal lines indicate *MLH* (green, *ML*) and *EZH* (pink, *EZ*) obtained from rawinsonde data. (For interpretation of the references to colour in this figure legend, the reader is referred to the web version of this article.)

not used in this analysis because, as mentioned previously, in both campaigns (summer and winter) the *MSP* lidar 2 was operated from 1000 *LT*.

4. Results and discussion

4.1. UBL properties based on rawinsonde measurements

Fig. 3 displays the seasonal variation of the statistical properties of *MLH* and *EZH* values estimated previously by Sánchez et al. (2020) from all 139 rawinsonde launching during the summer (February 19–28) and winter (August 6–15) field campaigns of 2013 in the *MRSP*. The mean and respective standard deviation of *EZ* thickness ($\overline{\Delta h}$), obtained from the difference between *EZH* and *MLH*, are also indicated.

During summer campaign, the mean values vary from a minimum of *MLH* = 347 ± 160 *m* and *EZH* = 487 ± 171 *m* at 0900 *LT* to a maximum of *MLH* = 1349 ± 443 *m* and *EZH* = 1552 ± 487 *m* at 1500 *LT*. During winter campaign, the mean values of *EZH* and *MLH* get smaller than summer campaign, varying from a minimum of *MLH* = 283 ± 142 *m* and *EZH* = 404 ± 179 *m* at 0900 *LT* to a maximum of *MLH* = 1038 ± 540 *m* and *EZH* = 1240 ± 580 *m* at 1500 *LT*. The time evolution of Δ*h* displays a similar diurnal and seasonal patterns, during summer (winter) the mean values of Δ*h* vary from a minimum of 120 ± 90 *m* (99 ± 43 *m*) at 0900 *LT* to a maximum of 174 ± 134 *m* (128 ± 100 *m*) at 1800 *LT* (1500 *LT*).

In summer the mean values of *EZH* and *MLH* at 1800 *LT* (1446 ± 693 and 1111 ± 649 *m*, respectively) are smaller than at 1500 *LT*. This unexpected behaviour is caused by sea breeze, that penetrates systematically during the afternoon, disrupting the normal course of *UBL* in the *MRSP* (Ribeiro et al., 2018; Sánchez et al., 2020). Besides, quite often the convective activity produces precipitation in the second half of the afternoon, that disrupts, mainly in summer, normal course of *UBL* evolution in the *MRSP*.

As expected, the mean values of *RLH* at 2100 *LT* vary from 1968 ± 253 *m* during summer to 1651 ± 335 m in winter campaign, following seasonal variation of the daytime evolution of *UBL* properties. Although the amplitude of the data distribution is smaller, *RLH* distributions around mean values are much more asymmetric than for *EZH* and *MLH*. This asymmetry is related to the fact that number of rawinsonde used to estimate *RLH* at 2100 LT (3 in each field campaign) is smaller than the number used to estimate *EZH* and *MLH* at 0900 *LT* (16 in summer and 15 in winter campaigns), and at 1200 *LT*, 1500 *LT* and 1800 *LT* (17 in each field campaigns).

4.2. Case studies

To illustrate how typical features of the *MRSP* local climate affect the performance of lidar methods, three case studies are analysed in detail: Case I: Winter clean atmosphere, Case II: Summer low clouds and aerosol multilayers, Case III: Summer sea-breeze intrusion.

After the case studies analysis, the performance of the seven lidar methods are objectively evaluated considering as reference *EZH* or *MLH*. The *PBLH* with the smallest average value of Δ_X is selected as reference. The performance is analysed using four metrics: *p-value* (*p*), $p < 0.05$ indicates the null hypothesis (*the mean PBLH values retrieved from lidar and rawinsonde measurements are equal)* is true to the significance level of 5%; Coefficient of determination (R^2), varies from 0 to 1 and indicates the fraction of the variance of the *PBLH* estimated by lidar that can be explained by the *PBLH* obtained by rawinsonde; Willmott index of agreement (*D*) (Willmott, 1981), varies also from 0 to 1 and indicates how lidar estimates of the *PBLH* are close to the rawinsonde ones; Root Mean Square Error (*RMSE*) measures the average deviation between *PBLH* estimates from lidar and rawinsonde. The best combination of these metrics, that will be used here to indicate the level of acceptability of a given lidar method, is $p < 0.05$, R^2 and *D* close to 1, and *RMSE* represents at most 10% of the reference *PBLH*.

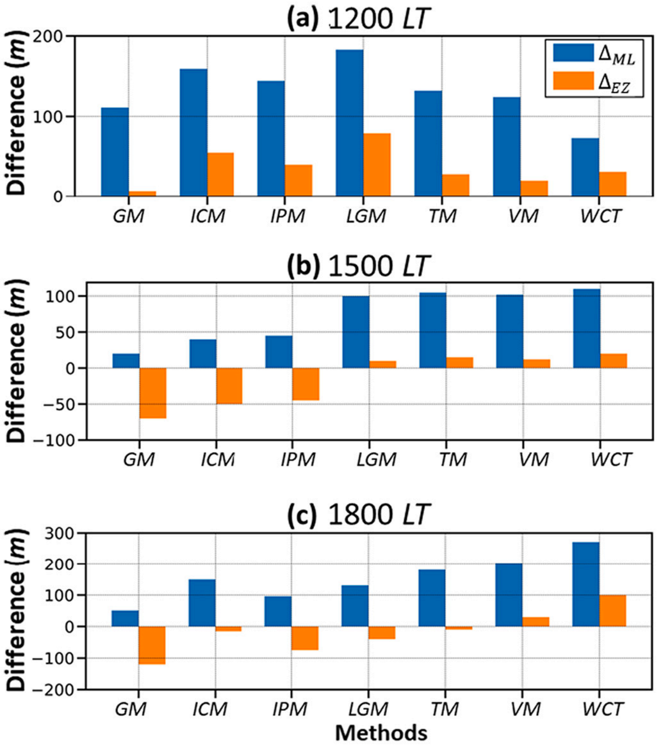

Fig. 5. Difference between *PBLH* estimated from lidar methods and rawinsonde at (a) 1200, (b) 1500 and (c) 1800 *LT* on August 11, 2013 (Case I – Winter clean atmosphere). The blue and orange bars indicate respectively Δ_{ML} and $\Delta_{EZ.}$ (*For interpretation of the references to colour in this figure legend, the reader is referred to the web version of this article.*)

Finally, the diurnal evolution of the *UBL* height and its local time rate of change estimated from the best lidar method are compared with rawinsonde estimates.

4.2.1. Case I – Winter clean atmosphere

On August 11, 2013, the passage of a cold front by the Brazilian shore affected the synoptic conditions in the *MRSP*. (Sánchez et al., 2020). Despite of the cold front, a well-defined *UBL* is identified by *RCS* contours map displayed in Fig. 4a. As expected for winter conditions in São Paulo (Section 4.1), the *UBL* presented a moderate growth reaching approximately 1200 *m* at 1500 *LT*.

From 1000 to 1600 *LT*, all seven lidar methods yielded similar values of *PBLH* (Fig. 4b) and close to the rawinsonde estimates (Fig. 4c). The homogeneity of *RCS* in the *UBL* region, as well as the absence of clouds and aerosol multilayers, facilitate the detection of the transition between *UBL* and *FA* (identified by strong reduction of the *RCS*). Similar results were observed by Zhong et al. (2020) in the presence of aerosol multilayers. The differences observed among lidar methods reflect their own definitions (Section 3.1) and do not exceed 150 *m*.

The discrepancy increases at 1700 *LT*, when aerosol multilayers appear. At 1800 *LT* the *WCT* indicates *PBLH* is above these layers, while the *VM* detected it close to the layer base located above the *EZH* (Fig. 4d). All the other methods estimate *PBLH* within the *EZ*. In the case of *WCT*, the distance between the top of *EZ* and the aerosol multilayers above (~70 *m*) is smaller than the Haar-function dilatation parameter (200 *m*). Consequently, *WCT* cannot differentiate these two regions because the vertical gradient does not appear in the covariance between the *RCS* profile and the Haar function. In the presence of aerosol multilayers above the *PBL*, Zhong et al. (2020) observed that *WCT* applied to lidar measurements, yields *PBLH* higher than estimated from rawinsonde data in Madison (*USA*), Southern Great Plains (*USA*), and Seoul

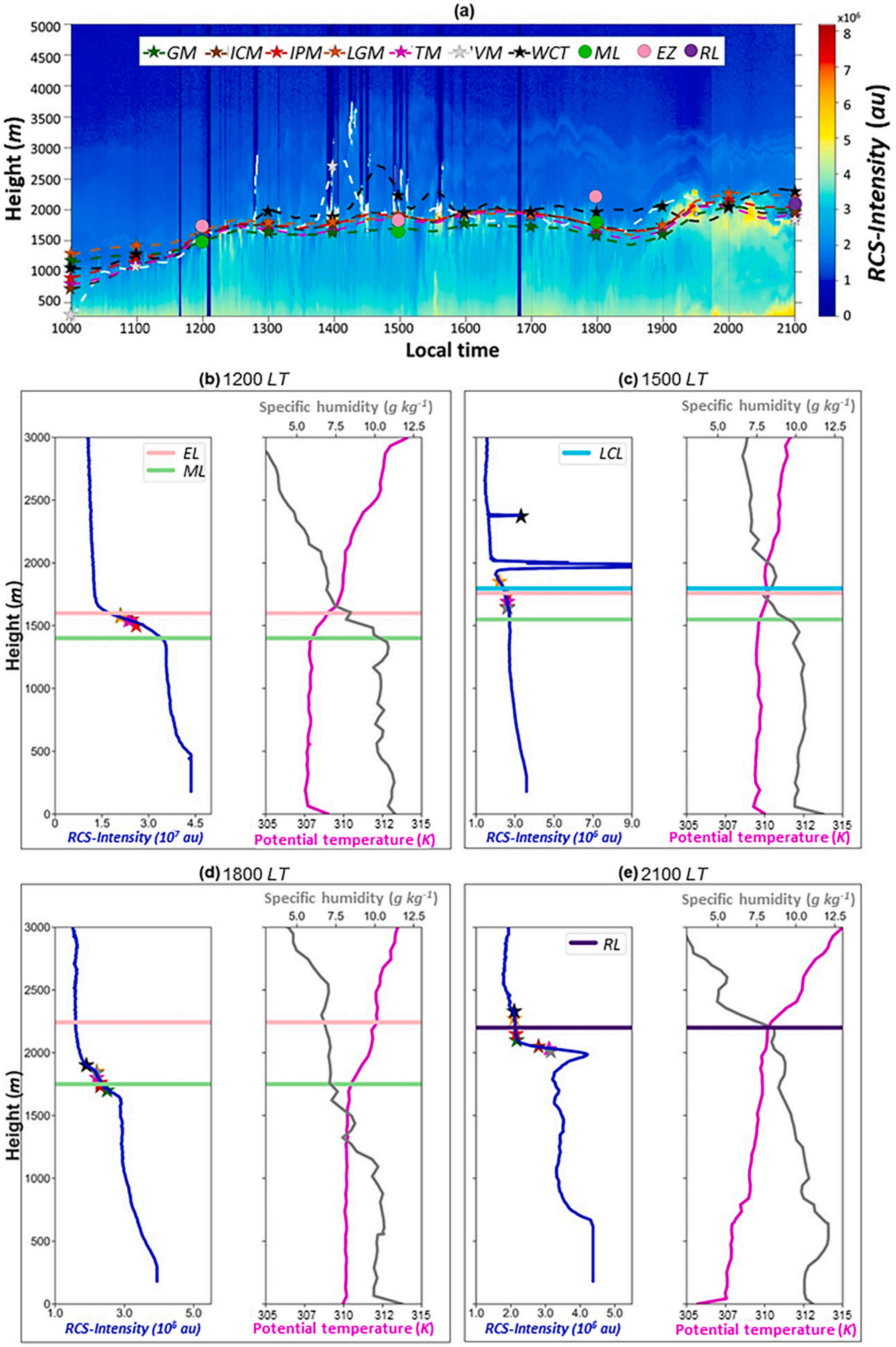

Fig. 6. (a) *RCS-Intensity* contour plot on February 21, 2013 (Case II - Summer low clouds and aerosol multilayers). The solid-star dashed-lines in (a) indicate *PBLHs* obtained from lidar methods, and solid circles indicate *MLH* (light green, *ML*), *EZH* (pink, *EZ*), and *RLH* (violet, *RL*) obtained from rawinsonde data. Vertical profiles of *RCS-Intensity* (blue line), potential temperature (magenta line) and specific humidity (grey line) in (b)- (e) correspond, respectively, to measurements at 1200, 1500, 1800 and 2100 *LT*. The solid stars in the *RCS-Intensity* profiles indicate *PBLHs* obtained from lidar methods, and horizontal lines indicate *MLH* (green, *ML*), *EZH* (pink, *EZ*) and *RLH* (violet, *RL*) obtained from rawinsonde data. The horizontal cyan line in (c) corresponds to *LCL* (Sánchez et al., 2020) (For interpretation of the references to colour in this figure legend, the reader is referred to the web version of this article.)

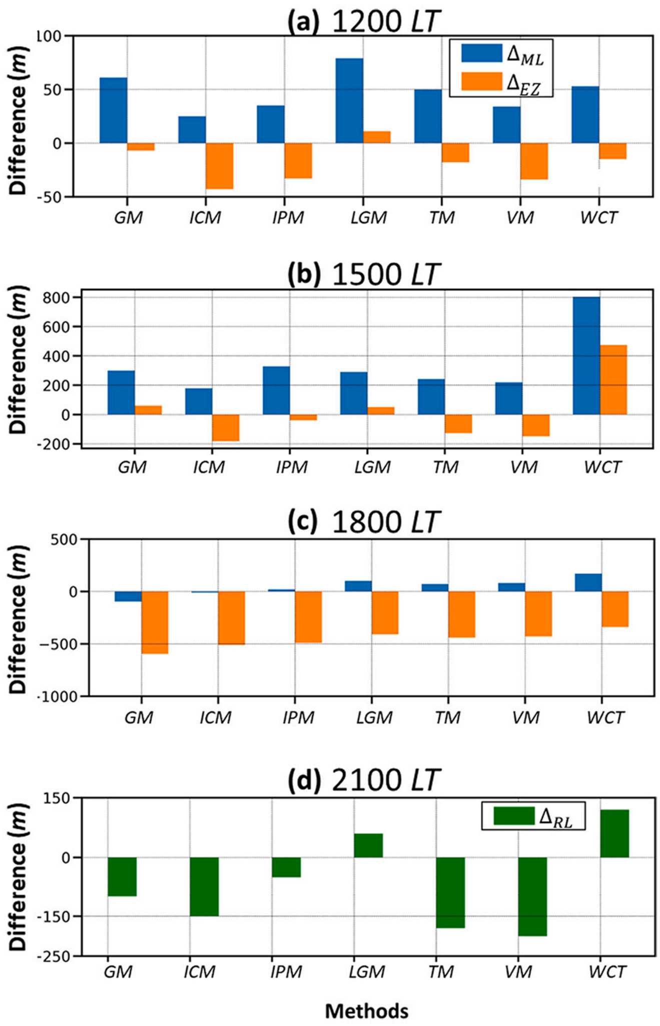

Fig. 7. Difference between *PBLH* estimated from lidar methods and rawinsonde at (a) 1200, (b) 1500, (c) 1800 and (d) 2100 *LT* on February 21, 2013 (Case II - Summer low clouds and aerosol multilayers). The blue, orange, and green columns indicate Δ_{ML}, Δ_{EZ} and Δ_{RL}, respectively

(Korea). In the case of *VM*, *PBLH* is overestimated because the aerosol multilayers above cause a local maximum in the variance profile of $\overline{RCS}$.

The time evolution of differences among *PBLH* retrieved from the seven lidar methods and rawinsonde are showed in Fig. 5. At 1200 *LT* (Fig. 5a), when the *UBL* has a fast-growing rate, these differences reach a maximum positive for all lidar methods, indicating that lidar overestimate systematically both *MLH* and *EZH*. At 1500 *LT* (Fig. 5b), after reaching the mature stage, the differences get smaller alternating negative and positive values. This is the expected behaviour since turbulent mixing homogenizes aerosol concentration reducing vertical gradients of *RCS* in the *UBL* (Fig. 5c). In accordance with their definitions, *ICM* and *IPM* retrieve *PBLH* within the *EZ*. *GM* also estimates the *PBLH* within the *EZ*, however, such a result is contrary to its definition which indicates $PBLH_{GM}$ in the *MLH*. The other four methods (*LGM*, *TM*, *VM*, and *WCT*) estimate *PBLH* above the *EZH*, disagreeing with their definitions. At 1800 *LT*, *ICM*, *IPM*, *GM* and *LGM* yield *PBLH* within the *EZ* (Fig. 5c). Again, only *ICM* and *IPM* are in accordance with their definition. *TM*, *VM*, and *WCT* estimate *PBLH* above the *EZH*, disagreeing with their definition.

4.2.2. *Case II – Summer low clouds and aerosol multilayers*

On February 21, 2013, prevailed in the *MRSP* synoptic conditions determined by the influence of an upper tropospheric cyclonic vortex positioned north-east of the *MRSP* (Sánchez et al., 2020). During summer, this synoptic system induces subsidence, favouring clear sky and strong solar heating of the surface. Combined with high moisture content of the atmosphere, this surface heating triggers convective activity increasing the presence of clouds in the *MRSP*, as observed during the afternoon on this day. These clouds are sparse and shallow, but their presence significantly increased the intensity of the signal received by the lidar system so that during cloud events *RCS* intensity is of the order of 10^7 *au*, at least one order of magnitude larger than clear sky conditions (Van Pul et al., 1994; Hennemuth and Lammert, 2006; Zhong et al., 2020). In this case (Fig. 6a), detecting the *UBL* structure is more complex than the previous case (Fig. 4a), mainly between 1230 and 1600 *LT* (Fig. 6a). Apart from this period, the *PBLH* retrieved by all lidar methods follow a similar pattern with standard deviation of 200 *m*.

During cloud activity periods, both *VM* (light grey solid-star dashed line in Fig. 6a) and *WCT* (black solid-star dashed line in Fig. 6a) yield *PBLH* values higher than all the other five lidar methods. These rather unrealistic high *PBLH* values occurred between 1230 and 1600 *LT* because *VM* and *WCT* are detecting the cloud base instead of the *PBLH* (Figs. 6c). For instance, at 1500 *LT*, the lifting condensation level (*LCL*) was 1797 *m*, while $PBLH_{WCT}$ was 2390 *m* (Fig. 6c). Similar difficulties in estimating the *PBLH* from lidar data in presence of clouds were described by Hennemuth and Lammert (2006), Toledo et al. (2017), Dang et al. (2019) and Zhong et al. (2020).

The time evolution of differences between *PBLH* retrieved from seven lidar methods and rawinsonde are showed in Fig. 7. At 1200 *LT* (Fig. 7a), all lidar methods estimate the *PBLH* within the *EZ*. In this layer, large vertical gradients in the aerosol load cause a sharp drop in the *RCS* profiles that seems to be equally detected by these seven methods. At 1500 *LT* (Fig. 7b), *GM* ($\Delta_{EZ} = 61$ *m*, $\Delta_{ML} = 300$ *m*), *LGM* ($\Delta_{EZ} = 51$ *m*, $\Delta_{ML} = 290$ *m*), and *WCT* ($\Delta_{EZ} = 475$ *m*, $\Delta_{ML} = 804$ *m*) overestimate *EZH* and *MLH*. The presence of low clouds causes multiple peaks in the *RCS* profile (Fig. 6c), making these three algorithms mislocate the *PBLH*, mainly gradient-based methods *GM* and *LGM*. The other four methods estimate the *PBLH* within *EZ*. At 1800 *LT* (Fig. 6c) all seven methods underestimate *EZH* ($-596 \le \Delta_{EZ} \le -340$ *m*) and yield *PBLH* closer *MLH* ($-96 \le \Delta_{ML} \le 170$ *m*). This behaviour is due to the presence of a large gradient in the *RCS* profile between 1700 and 1850 *m*.

Night-time lidar measurements are used here to determine the performance of the seven lidar methods in retrieving the top of the *RL*, using as reference rawinsonde estimates (*RLH*). At 2100 *LT* (Fig. 7d), *VM* ($\Delta_{RL} = -200$ *m*), *TM* ($\Delta_{RL} = -180$ *m*), ICM ($\Delta_{RL} = -150$ *m*), *GM* ($\Delta_{RL} = -100$ *m*), and *IPM* ($\Delta_{RL} = -50$ *m*), underestimate *RLH*, while *WCT* ($\Delta_{RL} = 120$ *m*) and *LGM* ($\Delta_{RL} = 60$ *m*) overestimate *RLH*. These discrepancies can be attributed to the presence of aerosol multilayers. They cause peaks in the *RCS* profiles (Fig. 6e) that are interpreted differently by the each retrieving methods. In this case, gradient-based methods (*GM*, *LGM*, and *IPM*) provided the best estimations of *RLH*. They detect more easily the region with high reduction in the *RCS* intensity (Fig. 6e).

4.2.3. *Case III – Summer sea-breeze intrusion*

On February 20, 2013, prevailed synoptic undisturbed conditions with clear sky associated to the subsidence induced by an upper tropospheric cyclonic vortex positioned north-east of the *MRSP* (Sánchez et al., 2020). The increment of cloudiness and aerosol concentration during the afternoon are associated with sea-breeze intrusions in the *MRSP*. Satellite and surface stations measurements (not displayed here) indicate that sea-breeze circulation was present in the *MRSP* during the afternoon and cloud cover was homogeneously distributed over the entire metropolitan region during this period.

Fig. 8a shows a well-defined *UBL* with a presence of clouds between 1400 and 1800 *LT*. From the beginning of measurements (1000 *LT*) until around 1430 *LT* the *UBL* exhibits a large growth rate, responding to the intense solar heating of surface during summer and under undisturbed conditions in the *MRSP*. Scattered clouds appear around 1400 *LT* and

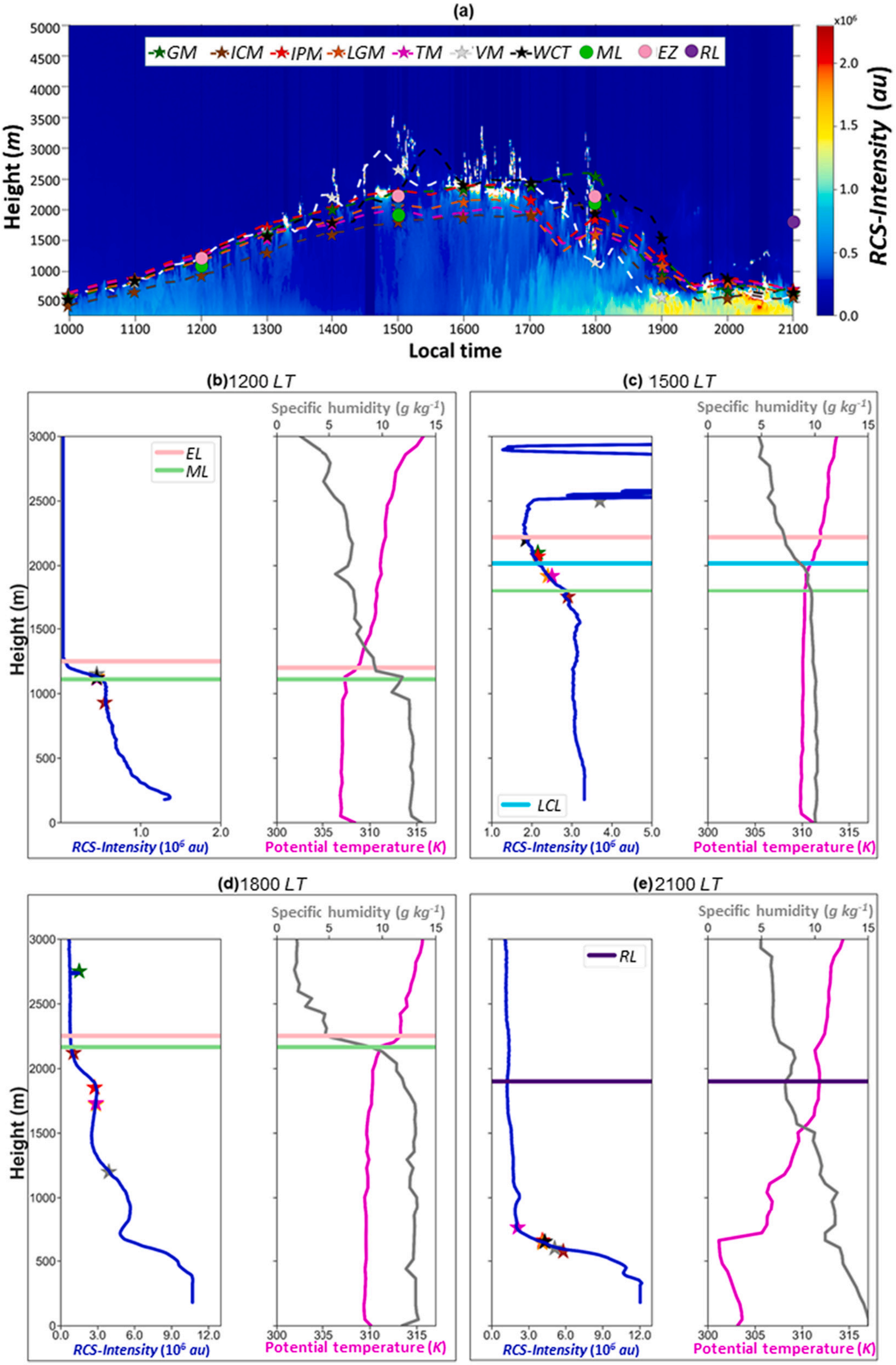

Fig. 8. (a) *RCS-Intensity* contour plot on February 20, 2013 (Case III – Summer sea-breeze intrusion). The solid-star dashed-lines in (a) indicate *PBLH*s obtained from lidar methods, and solid circles indicate *MLH* (light green, *ML*), *EZH* (pink, *EZ*), and *RLH* (violet, *RL*) obtained from rawinsonde data. Vertical profiles of *RCS-Intensity* (blue line), potential temperature (magenta line) and specific humidity (grey line) in (b)-(e) correspond, respectively, to measurements at 1200, 1500, 1800 and 2100 *LT*. The solid stars in the *RCS-Intensity* profiles indicate *PBLH*s obtained from lidar methods, and horizontal lines indicate *MLH* (green, *ML*), *EZH* (pink, *EZ*) and *RLH* (violet, *RL*) obtained from rawinsonde data. The horizontal cyan line in (c) corresponds to *LCL* (Sánchez et al., 2020) (For interpretation of the references to colour in this figure legend, the reader is referred to the web version of this article.)

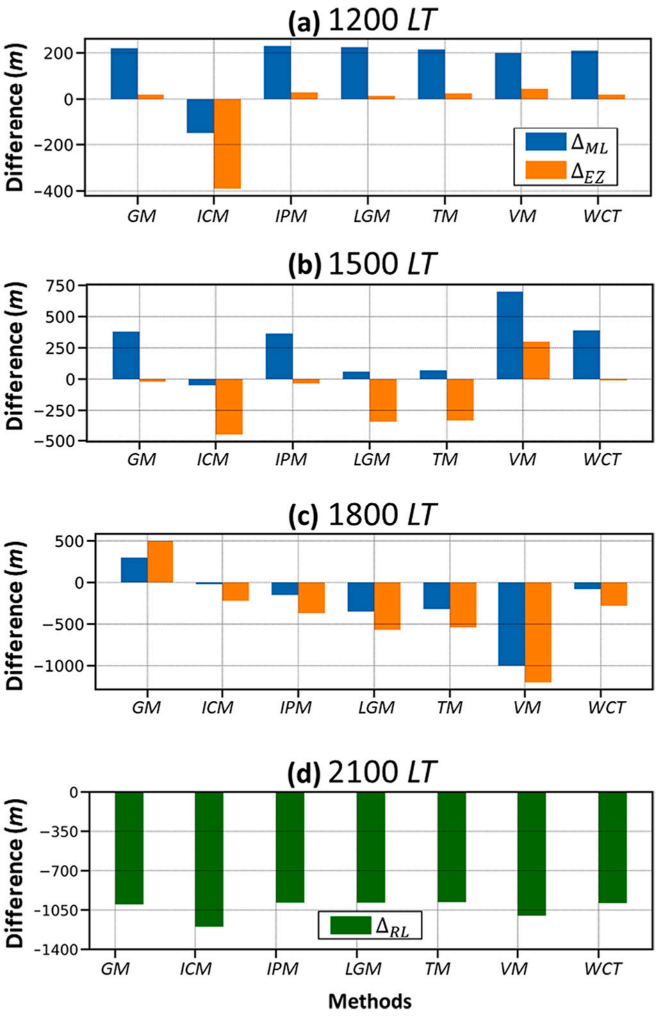

Fig. 9. Difference between *PBLH* retrieved from lidar methods and rawinsonde at (a) 1200, (b) 1500, (c) 1800 and (d) 2100 *LT* on February 21, 2013 (Case III – Summer sea-breeze intrusion). The blue and orange bars in (a)-(c) represent the difference between *MLH* (Δ_{ML}) and *EZH* (Δ_{EZ}) estimates. The green bars in (d) represent the difference between *RLH* (Δ_{RL}) retrieved from lidar methods and rawinsonde at (a) 2100 *LT* (For interpretation of the references to colour in this figure legend, the reader is referred to the web version of this article.)

increases significantly from 1600 *LT* on. There are indications that the *UBL* top surpasses cloud base height during this period. For instance, the *LCL* = 2017 *m* and *EZH* = 2219 *m* indicate the *UBL* top is about 200 *m* above the cloud base at 1500 *LT* (Fig. 8c). Differently from the previous case, the lidar measurements detected a very distinct aerosol layer in the first 700 *m* of the atmosphere from 1900 *LT* to 2100 *LT*.

During the period of fast *UBL* growth (1000 and 1400 *LT*), the transition between *UBL* and *FA* can be clearly seen in the *RCS* profiles (Fig. 8b), as consequence all lidar methods yield similar *PBLH* values. The only exception occurs around 1400 *LT* when a malfunction of the laser (unfortunately the laser reached the limit of useful life during this field campaign) makes the difference between the *RCS* in the *UBL* and *FA* region practically imperceptible (Fig. 8a). Between 1400 and 1700 *LT*, the differences among the methods increase because the *UBL* structure becomes more complex with the presence of clouds (Fig. 8c) within the *UBL* (Fig. 8d). As in the previous case studies, the presence of low clouds in the *UBL* is interpreted differently by each of the seven methods.

At 1800 *LT*, the presence of aerosol multilayers (900–1700 *m*) and a single cloud (2000–3000 *m*) cause multiple peaks in the *RCS* profile (Fig. 8d) leading all lidar methods retrieving divergent *PBLH* values (Fig. 8a). The progressive increase in the aerosol load below 700 *m* intensifies the contrast between high and low aerosol concentrations, improving the performance of all lidar methods after 1900 *LT* (Fig. 8a).

Fig. 9 shows the comparison among the *PBLH* obtained from lidar and rawinsonde data. At 1200 *LT*, *ICM* underestimated *EZH* and *MLH* ($\Delta_{EZ} = -390\ m$, $\Delta_{ML} = -150\ m$) due to the difficult of the algorithm in to find the inflexion point in the *RCS* profile. On the other hand, all the other six methods overestimate *EZH* ($20\ m \geq \Delta_{EZ} \geq 45\ m$) (Fig. 9a). Such overestimation is due to a large reduction in the *RCS* profile above the *EZ*. At 1500 *LT*, the presence of clouds increases the difference among lidar methods and *EZH* (Fig. 9b). Low values of *RCS* are the main reason for *ICM* to underestimate the *EZH* ($\Delta_{EZ} = -450\ m$) and *MLH* ($\Delta_{ML} = -50\ m$). The *VM* displays that largest difference, overestimating both *EZH* and *MLH* ($\Delta_{EZ} = 300$ m, $\Delta_{ML} = 700\ m$). In this case *VM* is estimating the height of the cloud base. The other five methods retrieve the *PBLH* within the *EZ*, with *GM* ($\Delta_{EZ} = -20\ m$, $\Delta_{ML} = 380$ m), *IPM* ($\Delta_{EZ} = -35\ m$, $\Delta_{ML} = 365\ m$) and *WCT* ($\Delta_{EZ} = -10\ m$, $\Delta_{ML} = 390\ m$) closer to *EZH*. *LGM* ($\Delta_{EZ} = -340\ m$, $\Delta_{ML} = 60\ m$) and *TM* ($\Delta_{EZ} = -330\ m$, $\Delta_{ML} = 70\ m$) yield *PBLH* closer to *MLH*. At 1800 *LT*, except for *GM* which estimate the *PBLH* in the base of the cloud (~ 2500 *m*), the other six methods underestimate the *EZH*. This behaviour is due to the presence of aerosol multilayers, which cause spikes in the *RCS* profiles masquerading the transition between *PBL* and *FA*.

As in the previous case study, night-time lidar measurements are used to assess the performance of all seven methods to retrieve *RLH*. At 2100 *LT* (Fig. 9d), all seven methods underestimated *RLH* by a larger difference ($-980\ m \geq \Delta_{RL} \geq -1200\ m$). However, differently from the previous case (Fig. 6a and e), on February 20 the *MRSP* was affected by the sea-breeze circulation, which brought maritime aerosol and moisture from Atlantic Ocean, affecting the lowest portion of the *UBL* during the afternoon (Sánchez et al., 2020). Therefore, instead of detecting the reduction in the *RCS* profile at the top of the *RL*, the contrast caused by a single aerosol layer (below 700 m), which was spawned by the sea-breeze intrusion (Fig. 8a and e). This result indicates that there are cases in the *MRSP*, mainly in the presence of sea-breeze circulation, when lidar measurements cannot be used to estimate the *RLH*, although all seven methods performed equally well in detecting the region of sharp decrease in the RCS profile.

4.3. *Assessing the best method for retrieving UBL height*

Although lidar methods are designed to detect *MLH* as a sharp drop in the *RCS* profile, this sharp drop is not always present and, as demonstrated in the previous sections, quite often is weakened, or even hidden by clouds and aerosol multilayers inside and above the *UBL* in the *MRSP*. In these cases, the *PBLH* is better identified by methods that explored other properties of the *RCS* profile. In this section the performance of seven lidar methods is assessed objectively using four metrics: *p*, R^2, *D*, and *RMSE*.

Table 1 displays a statistical analysis of summer and winter campaigns. At 1200 *LT* all methods have the average Δ_{EZ} values lower than the average Δ_{ML} values. *GM* has the best result (6.9 ± 3.2 *m*), while *LGM* has the worst (36.1 ± 17.1 *m*). At 1500 *LT TM* and *ICM* are closer to *MLH*, while in the other methods they are near to *EZH*. *GM* (−10.0 ± 3.2 *m*) and *WCT* (166.5 ± 43.2 *m*) have the best and worst results, respectively. At 1800 *LT GM*, *LGM* and *ICM* are close to the *EZH*, while in the others they are near to *MLH*. *IPM* has the best result (11.7 ± 4.1 *m*) and *VM* (246.9 ± 192.1 *m*) has the worst one.

For the three summer days (Table 2), at 1200 *LT* all methods are close to *EZH*, so that *GM* has the best estimative (10.2 ± 3.7 *m*) while *LGM* has the worst (42.0 ± 11.2 *m*). At 1500 *LT*, *TM* and *ICM* are close to *MLH* while in the others they are close to *EZH*. *GM* has the best result (−9.2 ± 2.3 *m*) and *WCT* (176.2 ± 55.2 *m*) has the worst. At 1800 *LT*, *GM*, *LGM* and, *ICM* are close to *EZH*, while in the others they are near to *MLH*. The best and worst results are provided by *WCT* (11.1 ± 3.7 *m*) and *VM* (143.2 ± 42.7 *m*), respectively.

For the eight winter days (Table 3), at 1200 *LT* all methods retrieved

Table 1
Mean and respective standard deviation of Δ_{EZ} and Δ_{ML} Lidar and rawinsonde measurements carried during summer (3 days) and winter (8 days) field campaigns of 2013 in the *MRSP*. The number of values is indicated by *n*. The green boxes represent best estimates of Δ_{EZ} and Δ_{ML}.

Method	Δ_{EZ} (*m*)			Δ_{ML} (*m*)		
	1200 *LT* (*n*=11)	1500 *LT* (*n*=11)	1800 *LT* (*n*=11)	1200 *LT* (*n*=11)	1500 *LT* (*n*=11)	1800 *LT* (*n*=11)
VM	10.6 ± 4.5	56.0 ± 18.1	-549.3 ± 530.2	122.9 ± 41.1	350.9 ± 210.2	246.9 ± 192.1
GM	6.9 ± 3.2	-10.0 ± 3.2	-74.2 ± 18.2	134.6 ± 51.2	240.3 ± 182.3	87.6 ± 27.2
LGM	36.1 ± 17.1	-95.8 ± 22.4	-35.0 ± 12.1	167.2 ± 42.1	154.5 ± 82.1	40.9 ± 17.2
IPM	12.7 ± 6.1	-41.2 ± 12.2	-32.1 ± 11.4	140.4 ± 32.0	253.7 ± 211.4	11.7 ± 4.1
TM	12.0 ± 5.3	-151.8 ± 47.3	-33.9 ± 11.8	136.3 ± 27.4	143.2 ± 44.2	23.7 ± 7.8
ICM	-11.9 ± 4.2	-234.2 ± 202.1	-25.8 ± 7.9	12.7 ± 4.2	58.0 ±12.1	41.2 ± 12.1
WTC	12.4 ± 5.3	166.5 ± 43.2	-17.8 ± 6.3	115.4 ± 39.8	447.7 ± 430.1	12.3 ± 3.9

Table 2
Mean and respective standard deviation of Δ_{EZ} and Δ_{ML} Lidar and rawinsonde measurements carried during summer (3 days) field campaigns of 2013 in the *MRSP*. The number of values is indicated by *n*. The green boxes represent best estimates of Δ_{EZ} and Δ_{ML}.

Method	Δ_{EZ} (*m*)			Δ_{ML} (m)		
	1200 *LT* (*n*=3)	1500 *LT* (*n*=3)	1800 *LT* (*n*=3)	1200 *LT* (*n*=3)	1500 *LT* (*n*=3)	1800 *LT* (*n*=3)
VM	12.4 ± 4.6	73.1 ± 21.3	-149.3± 82.4	127.8 ± 41.2	250.9 ± 215.4	143.2 ± 42.7
GM	10.2 ± 3.7	-9.2 ± 2.3	-70.2 ± 21.1	138.6 ± 43.2	260.2 ± 208.3	92.6 ± 30.1
LGM	42.0 ± 11.2	-82.3 ± 20.2	-30.0 ± 7.2	172.1 ± 52.1	162.5 ± 93.2	47.2 ± 15.2
IPM	15.3 ± 6.7	-22.1 ± 8.2	-30.1 ± 9.4	145.3 ± 43.4	223.6 ± 110.3	12.8 ± 4.2
TM	14.1 ± 5.3	-118.2 ± 25.3	-27.9 ± 6.8	146.1 ± 47.2	110.2 ± 42.3	25.7 ± 8.3
ICM	12.9 ± 3.2	-184.2 ± 62.4	-27.6 ± 7.3	138.2 ± 35.2	62.0 ± 20.1	40.3 ± 13.4
WTC	13.5 ± 4.1	176.2 ± 55.2	-20.3 ± 5.2	127.2 ± 32.3	432.7 ± 410.3	11.1 ± 3.7

PBLH close to *EZH*, so that the best and worst results are provided by *GM* (3.6 ± 0.7 *m*) and *ICM* (−36.7 ± 13.5 *m*), respectively. At 1500 *LT TM* and *ICM* are close to *MLH*, while in the others they are close to *EZH*. In this period *GM* has the best result (−10.8 ± 3.2 *m*) and *TM* (176.2 ± 62.3 *m*) the worst. At 1800 *LT GM*, *LGM* and *ICM* are close to *EZH*, while in the others they are close to *MLH*. *IPM* has the best (13.5 ± 4.7 *m*) while *VM* has the worst (370.6 ± 232.3 *m*).

Table 4 presents a summary of which region is best identified by the lidar methods in each one of the three analysed hours.

The performances of the seven lidar methods are indicated in Fig. 10. They are based on lidar and corresponding best rawinsonde estimates of *PBLH* (Table 4). The soundings which *PBLH* estimated are outliers in the boxplot diagram of Fig. 3 were removed from the performance analysis.

At 1200 *LT*, the *UBL* is in the growth stage. *GM*, *IPM*, *LGM*, and *VM* reject the null hypothesis (*p-value* ≥ 0.55) and have values of $R^2 \leq 0.6$, and *D* between 0.78 and 0.87. On the other hand, *ICM*, *TM*, and *WCT* present the best results (*p-value* < 0.05, $R^2 \geq 0.81$, *RMSE* < 266.70 *m*, and $D \geq 0.9$).

At 1500 *LT*, the *UBL* is fully developed. However, in the most of cases the vertical distribution of aerosol is complex due to presence of clouds. Except for *LGM* and *WCT*, which display an increase, all the other methods show a reduction in R^2. It occurs due to the presence of clouds and aerosol multilayers, which cause secondary peaks in the *RCS* profile confusing most of the *PBLH*-retrieving methods, so that only *LGM*, *TM* and *WCT* do not indicate the null hypothesis rejection. Similar problems were also observed in rural regions by Toledo et al. (2017) in Doñana National Park (Spain) and Dang et al. (2019) in Tsuiying Mountain in the Yuzhong campus of Lanzhou University (People's Republic of China). Consequently, there is an increase in the values of *RMSE* (mainly the *ICM*) and reduction of *D*. Although the increase in the values of *RMSE* also occurred with *LGM* and *WCT*, such methods provide better results, which can be verified by the values of $R^2 = 0.76$ (*LGM*) and 0.85 (*WCT*),

Table 3

Mean and respective standard deviation of Δ_{EZ} and Δ_{ML} Lidar and rawinsonde measurements carried during winter (8 days) field campaigns of 2013 in the *MRSP*. The number of values is indicated by *n*. The green boxes represent best estimates of Δ_{EZ} and Δ_{ML}.

Method	**Δ_{EZ} (*m*)**			**Δ_{ML} (m)**		
	1200 *LT* (*n*=8)	**1500 *LT* (*n*=8)**	**1800 *LT* (*n*=8)**	**1200 *LT* (*n*=8)**	**1500 *LT* (*n*=8)**	**1800 *LT* (*n*=8)**
VM	8.8 ± 2.5	38.9 ± 12.3	-939.3± 892.3	118.0 ± 40.3	450.9 ± 410.1	370.6 ± 232.3
GM	3.6 ± 0.7	-10.8 ± 3.2	-78.2 ± 22.4	130.6 ± 42.4	220.4 ± 198.3	82.6 ± 22.1
LGM	30.2 ± 9.8	-109.3 ± 35.2	-32.0 ± 12.3	162.3 ± 53.4	146.5 ± 92.2	34.6 ± 11.4
IPM	10.1 ± 3.4	-60.3± 19.4	-34.1 ± 11.2	135.5 ± 42.3	283.8 ± 185.4	10.6 ± 3.5
TM	9.9 ± 2.5	-185.4 ± 62.3	-39.9 ± 14.2	126.5 ± 44.2	176.2 ± 62.3	21.7 ± 7.2
ICM	-36.7 ± 13.5	-284.2 ± 192.4	-24.0 ± 7.8	-112.8 ± 35.7	54.0 ± 21.2	42.1 ± 12.5
WTC	11.3 ± 3.7	156.8 ± 52.3	-15.3 ± 5.2	103.6 ± 35.2	462.7 ± 420.5	13.5 ± 4.7

Table 4

The actual outcome of the *PBLH*-retrieving lidar methods. Discrepant outcomes are indicated by red.

Method	**Indicated for**	**Actual outcome**		
		1200 *LT*	**1500 *LT***	**1800 *LT***
VM	*MLH*	*EZH*	*EZH*	*MLH*
GM	*MLH*	*EZH*	*EZH*	*EZH*
LGM	*MLH*	*EZH*	*EZH*	*EZH*
IPM	*MLH - EZH*	*MLH - EZH*	*MLH - EZH*	*MLH - EZH*
TM	*MLH - EZH*	*MLH - EZH*	*MLH - EZH*	*MLH - EZH*
ICM	*MLH*	*EZH*	*EZH*	*EZH*
WTC	*MLH*	*EZH*	*EZH*	*MLH*

and $D = 0.94$ (for both methods).

At 1800 *LT* frequently occurs the transition from convective to stable regime in the *MRSP* (Sánchez et al., 2020). Excepting the *LGM* and *VM*, the other five lidar methods provide reliable results, so that the null hypothesis is not rejected. *LGM* and *VM* have the lower values of R^2 (lower than 0.6) and the higher *RMSE*, resulting in low reliability ($D < 0.77$). On the other hand, the *WCT* provides the best combination of results (high values of *D* and R^2, and low *RMSE*).

Based on the results described above, only *TM* and *WCT* results do not indicate the rejection of the null hypothesis in all periods evaluated (1200, 1500 and, 1800 *LT*). Therefore, they can be classified as the most reliable among the seven methods analysed here. Comparing the general performance of *WCT* and *TM* in terms of R^2, *D*, and *RMSE*, *WCT* ($R^2 = 0.86$, $D = 0.95$, $RMSE = 325.00\ m$) provides the best results in comparison to *TM* ($R^2 = 0.77$, $D = 0.92$, $RMSE = 325.70\ m$). Therefore, the method *WCT* can be selected as the reference lidar method that best retrieved the *PBLH* in the case of the *MRSP* and for an aerosol-lidar.

4.4. UBL properties based on lidar measurements

The diurnal evolution *PBLH* and its local time rate of change, based on lidar measurements carried out in the *MRSP* and retrieved by *WCT* method, are displayed in Fig. 11. They correspond to hourly values of *PBLH* averaged during 8 days in February and 3 days in August of 2013, respectively summer and winter field campaigns of *MCITY-BRAZIL* Project. By way of comparison, diurnal evolution of *PBLH* and its local rate of change are estimated using *PBLH* retrieved from rawinsonde carried out every three hours during the same 11 days by Sánchez et al. (2020). The region of the acceptable values delimited by the standard deviation of lidar estimates of *PBLH* (red and blue shadow in summer and winter, respectively) overlaps the region delimited by standard deviation (black and yellow vertical bars) of the hourly values of rawinsonde estimates of *PBLH*, reinforcing the agreement between them demonstrated in the previous section, once *PBLH* from rawinsonde correspond to *EZH*.

Even though these estimates are based on a reduced number of days (11) for any conclusive climatological analysis, they represent a

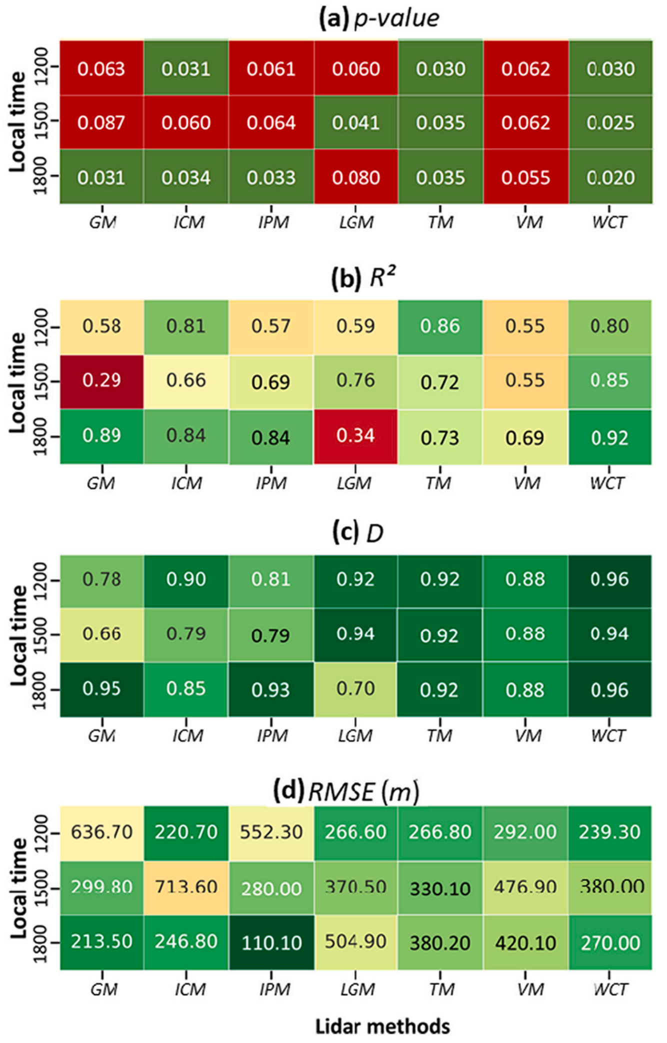

Fig. 10. Heat map of (a) *p-value*, (b) Coefficient of determination R^2, (c) Willmott index of agreement (*D*) and (d) Root mean square error (*RMSE*) for all lidar methods. The statistics displayed in each box is based on 11 *PBLH* values

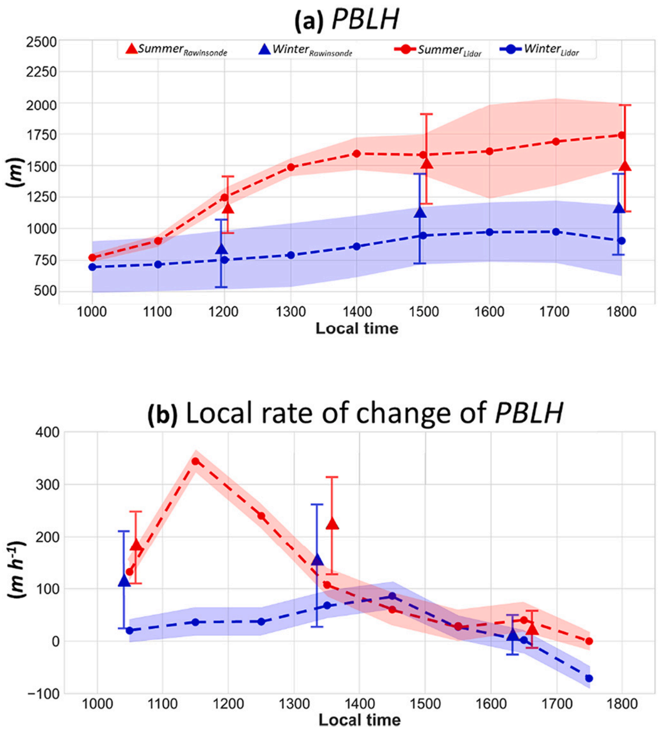

Fig. 11. Daytime evolution of hourly average values of (a) *PBLH* and (b) local rate of change of *PBLH* using lidar and rawinsonde measurements in the *MRSP*. Summer (red circle, black triangle) and Winter (blue circle, yellow triangle) values correspond to 3 and 8 days, respectively. Vertical bars and shadows indicated standard deviation of *PBLH* (For interpretation of the references to colour in this figure legend, the reader is referred to the web version of this article.)

significant number of soundings (47 rawinsondes, 169 10-min average *RCS* profiles), so that the agreement displayed by the average hourly values of *PBLH* retrieved from lidar and rawinsonde in both February (black triangles) and August (orange triangles) is desirable and, according to the hypothesis test performed in the previous section, significant. Both estimates of *PBLH* also showed the expected seasonal variation for *MRSP*, with the daytime evolution of *PBLH* during February (summer) systematically higher than in August (winter), a consequence of the seasonal variation of the surface heat flux and thermal stratification of the *FA* (Sánchez et al., 2020; Oliveira et al., 2020). This feature is particularly clear after noon time when the summer-winter difference varies from 600 *m* at 1200 *LT* to 850 *m* at 1800 *LT* (Fig. 11a). Marley et al. (2021), in Auckland (New Zealand), and Cimini et al. (2020), in Paris (France), also observed in urban regions higher values of *PBLH*, obtained from lidar data, in summer than winter.

The seasonal variation of local time rate of change of the *PBLH* retrieved by lidar is consistent with the one obtained from rawinsonde (Fig. 11b). During February, the lidar estimates varies from 132 to 344 $m\,h^{-1}$ between 1030 and 1230 *LT*. After this period, the local time rate of change begins to decrease, reaching the minimum value of 2 $m\,h^{-1}$ at 1800 *LT*. During August, the amplitude of the local time rate of change is smaller than during February, increasing from 20 to 86 $m\,h^{-1}$ between 1030 and 1430 *LT*. After this period, the local time rate of change decreases reaching 1 $m\,h^{-1}$ at 1630 *LT* and $-$ 69 $m\,h^{-1}$ at 1730 *LT*. The negative values appear due to the influence of the sea breeze, which affects the city of São Paulo in >50% of the days of the year (Oliveira et al., 2003). Such a phenomenon confines the aerosols in a single layer (with around 700 m) at the bottom of the *PBL*, so *WCT* method indicates a false reduction in the *PBLH*.

Despite the good agreement between lidar and rawinsonde estimates of *PBLH* (Fig. 11a), the diurnal evolution of the local time rate of change of *PBLH* has some significant differences in *MRSP* (Fig. 11b). During summer, the lidar and rawinsonde display a good agreement in both fast-growing and mature stages of the *UBL* development. However, during winter, local time rate of change of *PBLH* retrieved from lidar and rawinsonde agrees only during the mature stage of the *UBL*. During the fast-growing stage the local time rate of change of *PBLH* provided by rawinsonde is higher than lidar ones. The major reason for this discrepancy is the difference in temporal resolution of rawinsonde (3 h) and lidar (1 h), so that some variations registered by lidar systems cannot be properly detected by rawinsondes.

5. Conclusions

This paper describes a performance analysis of seven *PBLH*-detection lidar methods: Variance (VM), Gradient (GM), Logarithmic Gradient (LGM), Inflexion Point (IPM), Threshold (TM), (6) Ideal Curve-Fitting (ICM), and Wavelet Covariance Transform (WTC). The analysis used as reference *MLH, EZH* and *RLH* obtained previously by Sánchez et al. (2020) from rawinsonde data and *PBLH* retrieved from a mobile Raman lidar measurements carried out in the MRSP during two field campaigns of the *MCITY BRAZIL* Project in 2013 (Oliveira et al., 2020). It was assumed, based on the literature, that lidar methods *VM*, *GM*, *LGM*, *ICM*, *WCT* retrieve *PBLH* as the *MLH,* while *IPM* and *TM* retrieve as the centre of *EZ* layer. It was assumed also that all seven methods are equally capable to retrieve *RLH* because no information was available in the literature.

Analysis of the three selected cases demonstrated how *PBL* heights retrieved from lidar data respond to typical meteorological scenarios observed in the MRSP during field campaigns of 2013.

Under undisturbed conditions observed during winter (case I), all methods retrieved *PBL* heights in agreeing to their definition during daytime. Similar results were observed by Zhong et al. (2020) in the presence of aerosol multilayers. The differences observed among lidar methods reflect their own definitions (Section 3.1) and do not exceed 150 *m*. Therefore, good matching between *UBL* properties retrieved by lidar and rawinsonde measurements indicate that undisturbed conditions visual inspection and all seven lidar methods have similar accuracy.

During daytime and under more disturbed synoptic conditions (cases II and II) the *PBL* height retrieved by lidar methods are mostly close to *EZH*, disagreeing of the *PBLH* definition adopted by these lidar methods. This occurs because the expected gradual above-*ML* reduction in the aerosol concentration happens more sharply above the *EZ* in the *MRSP,* resulting in a sharp drop in the *RCS* profile in this region.

During night-time and in the absence of sea-breeze intrusions (case II), the *RL* heights obtained by all lidar methods agree with *RLH*. On the hand, the sea-breeze intrusion (case III) increases aerosol concentration in lower portion of the atmosphere, causing a sharp drop in the RCS profile below the *SIH* and all lidar methods grossly underestimate *RLH*. Due to the 180-m overlap of MSP-2, lidar measurements during night-time could not be used to estimate the *SBLH*, because maximum *SBLH* reached, on average, 126 ± 13 m in February and 122 ± 10 m in August field campaigns (Sánchez et al., 2020). Even though the maximum *SIH* varied, on average, from 322 ± 80 m in February to 326 ± 74 m in August field campaigns (Sánchez et al., 2020), all attempts to estimate *SIH* in the *RMSP* using lidar measurements failed because, during the 2013 field campaigns, the vertical aerosol distribution showed no detectable variation along the transition between of the *SI* layer top and *RL* bottom.

From statistical analysis, during the fast-growing stage (1200 *LT*), the algorithms *WCT*, *ICM* and *TM* provide very reliable results (*p-value* < 0.05, $R^2 \geq 0.81$, $RMSE < 267.00$ *m* and $D \geq 0.90$). When the *UBL* reaches the mature stage (1500 *LT*), the cases without clouds characterize the simplest situation, so that *LGM*, *TM* and *WCT* provide the more accurate results (*p-value* < 0.05, $R^2 \geq 0.72$, $RMSE \leq 380.00$ *m* and $D \geq 0.92$). During the convective-stable transition stage (1800 *LT*), the best results are provided by *WCT* (*p-value* < 0.05, $R^2 = 0.90$, $RMSE = 290.70$ *m*, and $D = 0.94$). On the other hand, The *IPM* method provides the best results of *RL* height during a typical summer night in the *MRSP*.

The highest performance of *WCT*, indicated by *p-value* < 0.05, R^2 and *D* close to 1, and *RMSE* lower than 10%, indicate that comparatively to all the other six lidar methods, *WCT* method is the most recommend lidar method for estimating *UBL* height in the *MRSP*.

The analysis performed in this work corroborate that lidar measurements has a positive impact on improving the ability to describe the diurnal evolution of the *UBL* growth rate, increasing the temporal and spatial resolution of the rawinsonde base estimates. However, as demonstrated also, any objective interpretation of lidar measurements requires a validation of the retrieving method to the local climate conditions. In regions with climate like the *MRSP* it is necessary to take int consideration the combined effects of low clouds and sea-breeze circulation on the vertical distribution aerosol within and above the *UBL*. It was demonstrated here, even when a second independent estimate of the *PBL* height is available (like rawinsonde) the strategy to avoid the misinterpretation of lidar results are extremely dependent on the previously knowledge of the local pattens of aerosol distribution what is rarely available in most of the places.

CRediT authorship contribution statement

Gregori de Arruda Moreira: Conceptualization, Methodology, Software, Data curation, Writing – original draft, Investigation. **Amauri Pereira de Oliveira:** Conceptualization, Writing – review & editing, Investigation, Supervision. **Maciel Piñero Sánchez:** Data curation, Investigation. **Georgia Codato:** Data curation, Investigation. **Fábio Juliano da Silva Lopes:** Data curation, Investigation. **Eduardo Landulfo:** Supervision. **Edson Pereira Marques Filho:** Supervision.

Declaration of Competing Interest

The authors declare that they have no known competing financial interests or personal relationships that could have appeared to influence the work reported in this paper.

Acknowledgements

This research was sponsored by CNPq (309079/2013-6, 305357/2012-3, 462734/2014-5, 304786/2018-7; 154320/2018-8, 304786/2018-7) FAPESP (2011/50178-5), FAPERJ (E26/111.620/2011, E26/103.407/2012) and CAPES (CAPES Financial Code 001).

References

Antuña-Marrero, J.C., Landulfo, E., Estevan, R., Barja, B., Robock, A., Wolfram, E., Ristori, P., Clemesha, B., Zaratti, F., Forno, R., Armandillo, E., Bastidas, A.E., de Frutos Baraja, A.M., Whiteman, D.N., Quel, E., Barbosa, H.M.J., Lopes, F., Montilla-Rosero, E., Guerrero-Rascado, J.L., 2017. LALINET: the first Latin American-born regional atmospheric observational network. Bull. Am. Meteorol. Soc. 98, 1255–1275.

Baars, H., Ansmann, A., Engelmann, R., Althausen, D., 2008. Continuous monitoring of the boundary-layer top with lidar. Atmos. Chem. Phys. 8 (3), 10749–10790.

Banks, R.F., Tiana-Alsina, J., Baldasano, J.M., Rocadenbosch, F., Papayannis, A., Solomos, S., Tzanis, C.G., 2016. Sensitivity of boundary-layer variables to PBL schemes in the WRF model based on surface meteorological observations, lidar, and radiosondes during the HygrA-CD campaign. Atmos. Res. 185–201.

Bianco, L., Wilczak, J.M., 2002. Convective boundary layer depth: improved measurement by doppler radar wind profiler using Fuzzy logic methods. J. Atmos. Ocean. Technol. 19 (11), 1745–1758.

Boers, R., Spinhirne, J.D., Hart, W.D., 1988. Lidar observations of the fine-scale variability of marine stratocumulus clouds. J. Appl. Meteorol. 27, 797–810.

Bonin, T.A., Carroll, B.J., Hardesty, R.M., Brewer, W.A., Hajny, K., Salmon, O.E., Shepson, P.B., 2018. Doppler lidar observations of the mixing height in Indianapolis using an automated composite Fuzzy logic approach. J. Atmos. Ocean. Technol. 35 (3), 473–490.

Bravo-Aranda, J.A., de Arruda Moreira, G., Navas-Guzmán, F., Granados-Muñoz, M.J., Guerrero-Rascado, J.L., Pozo-Vázquez, D., Arbizu-Barrena, C., Olmo-Reyes, F.J., Mallet, M., Alados-Arboledas, L., 2017. A new methodology for PBL height estimations based on lidar depolarization measurements: analysis and comparison against MWR and WRF model-based results. Atmos. Chem. Phys. 17, 6839–6851.

Brooks, I.M., 2003. Finding boundary layer top: application of a wavelet covariance transform to lidar backscatter profiles. J. Atmos. Ocean. Technol. 20 (8), 1092–1105.

Cazorla, A., Casquero-Vera, J.A., Román, R., Guerrero-Rascado, J.L., Toledano, C., Cachorro, V.E., Orza, J.A.G., Cancillo, M.L., Serrano, A., Titos, G., Pandolfi, M., Alastuey, A., Hanrieder, N., Alados-Arboledas, L., 2017. Near-real-time processing of a ceilometer network assisted with sun-photometer data: monitoring a dust outbreak over the Iberian Peninsula. Atmos. Chem. Phys. 17, 11861–11876. https://doi.org/10.5194/acp-17-11861-2017.

Cimini, D., Haeffelin, M., Kotthaus, S., Löhnert, U., Martinet, P., O'Connor, E., Walden, C., Coen, M.C., Preissler, J., 2020. Towards the profiling of the atmospheric boundary layer at European scale—introducing the COST Action PROBE. Bull. Atmos. Sci. Technol. 1, 23–42. https://doi.org/10.1007/s42865-020-00003-8.

D'Amico, G., Amodeo, A., Mattis, I., Freudenthaler, V., Pappalardo, G., 2016. EARLINET single calculus chain—Technical—Part 1: pre-processing of raw lidar data. Atmos. Meas. Tech. 9, 491–507. https://doi.org/10.5194/amt-9-491-2016.

Dang, R., Yang, Y., Hu, X.M., Wang, Z., Zhang, S., 2019. A review of techniques for diagnosing the atmospheric boundary layer height (ABLH) using aerosol lidar data. Remote Sens. 11, 1590. https://doi.org/10.3390/rs11131590.

Davis, K.J., Gamage, N., Hagelberg, C.R., Kiemle, C., Lenschow, D.H., Sullivan, P.P., 2000. An objective method for deriving atmospheric structure from airborne lidar observations. J. Atmos. Ocean. Technol. 17 (11), 1455–1468.

De Tomasi, F., Miglietta, M.M., Perrone, M.R., 2011. The growth of the planetary boundary layer at a coastal site: a case study. Boundary-Layer Meteorol. 139 (3), 521–541.

Emeis, S., 2011. Surface-based remote sensing of the atmospheric boundary layer. Springer.

Flamant, C., Pelon, J., Flamant, P.H., Durand, P., 1997. Lidar determination of the entrainment zone thickness at the top of the unstable marine atmospheric boundary layer. Boundary-Layer Meteorol. 83, 247–284.

Frioud, M., Mitev, V., Matthey, R., Häberli, C.H., Richner, H., Werner, R., Vogt, S., 2003. Elevated aerosol stratification above the Rhine Valley under strong anticyclonic conditions. Atmos. Environ. 37, 1785–1797.

Granados-Muñoz, M.J., Navas-Guzmán, F., Bravo-Aranda, J.A., Guerrero-Rascado, J.L., Lyamani, H., Fernández-Gálvez, J., Alados-Arboledas, L., 2012. Automatic determination of the planetary boundary layer height using lidar: one-year analysis over southeastern Spain. J. Geophys. Res. Atmos. 117 (D18).

Guerrero-Rascado, J., Landulfo, E., Antuña, J., de Melo Jorge Barbosa, H., Barja, B., Bastidas, Á., Bedoya, A., da Costa, R., Estevan, R., Forno, R., Gouveia, D., Jiménez, C., Larroza, E., da Silva Lopes, F., Montilla-Rosero, E., de Arruda Moreira, G., Nakaema, W., Nisperuza, D., Alegria, D., Múnera, M., Otero, L., Papandrea, S., Pallota, J., Pawelko, E., Quel, E., Ristori, P., Rodrigues, P., Salvador, J., Sánchez, M., Silva, A., 2016. Latin American Lidar Network (LALINET) for aerosol research: diagnosis on network instrumentation. J. Atmos. Sol-Terr. Phy. 138–139, 112–120.

Hennemuth, B., Lammert, A., 2006. Determination of the atmospheric boundary layer height from radiosonde and lidar backscatter. Boundary-Layer Meteorol. 120 (1), 181–200.

Holzworth, G.C., 1964. Estimates of mean maximum mixing depths in the contiguous United States. Mon. Weather Rev. 92, 235–242.

Kotthaus, S., O'Connor, E., Münkel, C., Charlton-Perez, C., Haeffelin, M., Gabey, A.M., Grimmond, C.S.B., 2016. Recommendations for processing atmospheric attenuated backscatter profiles from Vaisala CL31 ceilometers. Atmos. Meas. Tech. 9, 3769–3791. https://doi.org/10.5194/amt-9-3769-2016.

Kotthaus, S., Haeffelin, M., Drouin, M.A., Dupont, J.C., Grimmond, S., Haefele, A., Hervo, M., Poltera, Y., Wiegner, M., 2020. Tailored algorithms for the detection of the atmospheric boundary layer height from Common Automatic Lidars and Ceilometers (ALC). Remote Sens. 12, 3259. https://doi.org/10.3390/rs12193259.

Kovalev, A.V., Eichinger, E.W., 2004. Elastic Lidar: Theory, Practice and Analysis Methods. Willey Interscience.

Lange, D., Tiana-Alsina, J., Saeed, U., Tomás, S., Rocadenbosch, F., 2014. Using a Kalman filter and backscatter lidar returns. IEEE Trans. Geosci. Remote Sens. 52 (8), 4717–4728.

Liu, B., Ma, Y., Gong, W., Zhang, M., Yang, J., 2019. Improved two-wavelength Lidar algorithm for retrieving atmospheric boundary layer height. J. Quant. Spectrosc. Radiat. Transf. 224, 55–61.

Lopes, F.J.S., Moreira, G.A., Rodrigues, P.F., Guerrero-Rascado, J.L., Andrade, M.F., Landulfo, E., 2014. Comparison between two algorithms based on different wavelets to obtain the planetary boundary layer height. In: Proc. SPIE 9246, Lidar Technologies, Techniques, and Measurements for Atmospheric Remote Sensing X, 92460H.

Marley, H.G., Dirks, K.N., McKendry, I., Weissert, L.F., Salmond, J.A., 2021. A ceilometer-derived climatology of the convective boundary layer over a Southern hemisphere subtropical city. Boundary-Layer Meteorol. 178, 435–462. https://doi.org/10.1007/s10546-020-00579-w.

Martucci, G., Matthey, R., Mitev, V., Richner, H., 2007. Comparison between backscatter lidar and radiosonde measurements of the diurnal and nocturnal stratification in the lower troposphere. J. Atmos. Ocean. Technol. 24 (7), 1231–1244.

Melfi, S.H., Spinhirne, J.D., Chou, S.H., Palm, S.P., 1985. Lidar observations of vertically organized convection in the planetary boundary layer over the ocean. J. Appl. Meteorol. Climatol. 24 (8), 806–821.

Menut, L., Flamant, C., Pelon, J., Flamant, P.H., 1999. Urban boundary layer height determination from lidar measurements over the Paris area. Appl. Opt. 38, 945–954.

Moreira, G.A., Bourayou, R., Lopes, F.J.S., Albuquerque, T.A., Reis Jr., N.C., Held, G., Landulfo, E., 2013. Automatic methods to detect the top of atmospheric boundary layer. In: Proc. SPIE 8894, Lidar Technologies, Techniques, and Measurements for Atmospheric Remote Sensing IX, 88940T. https://doi.org/10.1117/12.2028750.

Moreira, G.A., Lopes, F.J.S., Guerrero-Rascado, J.L., Granados-Muñoz, M.J., Bourayou, R., Landulfo, E., 2014. Comparison between two algorithms based on different wavelets to obtain the Planetary Boundary Layer height. In: Proc. SPIE 9246, Lidar Technologies, Techniques, and Measurements for Atmospheric Remote Sensing X, 92460D. https://doi.org/10.1117/12.2067352.

Moreira, G.A., Guerrero-Rascado, J.L., Benavent-Oltra, J.A., Ortiz-Amezcua, P., Román, R., Bedoya- Velásquez, A.E., Bravo-Aranda, J.A., Olmo-Reyes, F.J., Landulfo, E., Alados-Arboledas, L., 2018. Analyzing the turbulence in the Planetary Boundary Layer by the synergic use of remote sensing systems: Doppler wind lidar and aerosol elastic lidar. Atmos. Res. 213, 185–195.

Moreira, G.A., Guerrero-Rascado, J.L., Benavent-Oltra, J.A., Ortiz-Amezcua, P., Román, R., Bedoya- Velásquez, A.E., Bravo-Aranda, J.A., Olmo-Reyes, F.J., Landulfo, E., Alados-Arboledas, L., 2019. Analyzing the turbulent planetary boundary layer by remote sensing systems: the Doppler wind lidar, aerosol elastic lidar and microwave radiometer. Atmos. Chem. Phys. 19, 1263–1280.

Moreira, G.A., Guerrero-Rascado, J.L., Bravo-Aranda, J.A., Foyo-Moreno, I., Cazorla, A., Alados, I., Lyamani, H., Landulfo, E., Alados-Arboledas, L., 2020. Study of the planetary boundary layer height in an urban environment using a combination of microwave radiometer and ceilometer. Atmos. Res. 240, 104932 https://doi.org/10.1016/j.atmosres.2020.104932.

Moreira, G.d.A., Oliveira, A.P.d., Codato, G., Sánchez, M.P., Tito, J.V., Silva, L.A.H., Silveira, L.C.d., Silva, J.J., Lopes, F.J.d.S., Landulfo, E., 2022. Assessing spatial variation of PBL height and aerosol layer aloft in São Paulo megacity using simultaneously two lidar during Winter 2019. Atmosphere 13 (4), 611. https://doi.org/10.3390/atmos13040611.

Morille, Y., Haeffelin, M., Drobinski, P., Pelon, J., 2007. STRAT: an automated algorithm to retrieve the vertical structure of the atmosphere from single-channel lidar data. J. Atmos. Ocean. Technol. 24 (5), 761–775.

Oliveira, A.P., Bornstein, R., Soares, J., 2003. Annual and diurnal wind patterns in the city of Sao Paulo. Water Air Soil Pollut. 3, 3–15. https://doi.org/10.1023/A:1026090103764.

Oliveira, A.P., Marques Filho, E.P., Ferreira, M.J., Codato, G., Ribeiro, F.N.D., Landulfo, E., Moreira, G.A., Pereira, M.M.R., Mlakar, P., Boznar, M.Z., Assis, E.S., Ferreira, D.G., Cassol, M., Escobedo, J.F., Dal Pai, A., França, J.R.A., Quintão, D.A., Rabelo, F.D., Souza, L.A.T., Silva, W.P., Domingues, L.M., Sánchez, M.P., Silveira, L. C., Vito, J.V., 2020. Assessing urban effects on the climate of metropolitan regions of Brazil - preliminary results of the MCITY BRAZIL project. Explor. Environ. Sci. Res. 1 (1), 38–77. https://doi.org/10.47204/EESR.1.1.2020.038-077.

Pal, S., Behrendt, A., Wulfmeyer, V., 2010. Elastic-backscatter-lidar-based characterization of the convective boundary layer and investigation of related statistics. Ann. Geophys. 28 (3), 825–847.

Ribeiro, F.N.D., Oliveira, A.P., Soares, J., Miranda, R.M., Barlage, M., Chen, F., 2018. Effect of sea breeze propagation on the urban boundary layer of the metropolitan region of Sao Paulo, Brazil. Atmos. Res. 214, 174–188. https://doi.org/10.1016/j.atmosres.2018.07.015.

Sánchez, M.P., Oliveira, A.P., Varona, R.P., Tito, J.V., Codato, G., Ribeiro, F.N.D., Marques Filho, E.P., Silveira, L.C., 2020. Rawinsonde-based analysis of the urban boundary layer in the metropolitan region of São Paulo, Brazil. Earth Space Sci. 7 https://doi.org/10.1029/2019EA000781 e2019EA000781.

Senff, C.J., Bösenberg, J., Peters, G., Schaberl, T., 1996. Remote sensing of turbulent ozone fluxes and the ozone budget in the convective boundary layer with DIAL and radar-RASS: a case study. Atmos. Phys. 69, 161–176.

Steyn G., D., Baldi, M., Hoff M., R., 1999. The detection of mixed layer depth and entrainment zone thickness from Lidar backscatter profiles. J. Atmos. Ocean. Technol. 16, 953–959. https://doi.org/10.1175/1520-0426(1999)016<0953:TDOMLD>2.0.CO;2.

Stull, R.B., 1988. An Introduction to Boundary Layer Meteorology. Kluwer, Dordrecht.

Toledo, D., Córdoba-Jabonero, C., Adame, J.A., Morena, B., Gil-Ojeda, M., 2017. Estimation of the atmospheric boundary layer height during different atmospheric conditions: a comparison on reliability of several methods applied to lidar measurements. Int. J. Remote Sens. 38 (11), 3203–3218. https://doi.org/10.1080/01431161.2017.1292068.

Tucker, S.C., Senff, C.J., Weickmann, A.M., Brewer, W.A., Banta, R.M., Sandberg, S.P., Law, D.C., Hardesty, R.M., 2009. Doppler lidar estimation of mixing height using turbulence, shear, and aerosol profiles. J. Atmos. Ocean. Technol. 26 (4), 673–688.

Van Pul, W.A.J., Holtslag, A.A.M., Swart, D.P.J., 1994. A comparison of ABL heights inferred routinely from lidar and radiosondes at noontime. Boundary-Layer Meteorol. 68, 173–191. https://doi.org/10.1007/BF00712670.

Vishnu, R., Kumar, Y.B., Nair, A.K.M., 2021. An investigation of the elevated aerosol layer using a polarization lidar over a tropical rural site in India. Boundary-Layer Meteorol. 178, 323–340. https://doi.org/10.1007/s10546-020-00573-2.

Wang, Z., Cao, X., Zhang, L., Notholt, J., Zhou, B., Liu, R., Zhang, B., 2012. Lidar measurement of planetary boundary layer height and comparison with microwave profiling radiometer observation. Atmos. Meas. Tech. 5 (8), 1965–1972.

Willmott, C.J., 1981. On the validation of models. Phys. Geogr. 2, 184–194. https://doi.org/10.1080/02723646.1981.10642213.

Wyngaard, J.C., 2010. Turbulence in the Atmosphere. Cambridge University Press, Cambridge, UK.

Zhang, Y., Seidel, D.J., Zhang, S., 2013. Trends in planetary boundary layer height over Europe. J. Clim. 26, 10071–10076. https://doi.org/10.1175/JCLI-D-13-00108.

Zhong, T., Wang, N., Shen, X., Xiao, D., Xiang, Z., Liu, D., 2020. Determination of planetary boundary layer height with lidar signals using maximum limited height initialization and range restriction (MLHI-RR). Remote Sens. 12, 2272. https://doi.org/10.3390/rs12142272.